

# Microstructural study of keyhole TIG welded nickel-based superalloy G27

Achmad Ariaseta<sup>a,d,\*</sup>, Abdul Khaliq Khan<sup>c</sup>, Joel Andersson<sup>a</sup>, Olanrewaju Ojo<sup>b</sup>

<sup>a</sup> Department of Engineering Science, University West, SE-46186 Trollhättan, Sweden

<sup>b</sup> Department of Mechanical Engineering, University of Manitoba, Winnipeg, MB R3T 5V6, Canada

<sup>c</sup> Manitoba Institute for Materials, University of Manitoba, Winnipeg, MB R3T2N2, Canada

<sup>d</sup> Department of Metallurgical Engineering, Faculty of Mining and Petroleum Engineering, Institut Teknologi Bandung, Jl. Ganesha 10, Bandung 40132, Indonesia

## ARTICLE INFO

### Keywords:

K-TIG welding  
Weld solidification  
Laves phase  
Grain growth  
G27  
Superalloy

## ABSTRACT

The weld fusion zone (FZ) microstructure obtained after keyhole tungsten inert gas welding and post-weld solution heat treatments (PWSHTs) of a new nickel (Ni)-based superalloy called G27 is studied, and the grain growth behavior in the base material (BM) during PWSHTs is characterized. Microsegregation-induced interdendritic microconstituents in the FZ of as-welded G27 are identified by analytical (scanning) transmission electron microscopy ((S)TEM) as niobium (Nb)-rich MC carbides, Nb-rich Laves eutectic constituents,  $\gamma'$  and  $\eta$  phases. The Laves eutectics are generally considered brittle and can adversely affect the mechanical properties of the weldment; thus, an hour PWSHTs were performed at 954 °C–1060 °C to eliminate the  $\gamma$ /Laves eutectics. PWSHT up to 1010 °C results in only partial removal of Laves eutectics with an excessive formation of  $\eta$  phase surrounding the Laves phase. Complete dissolution of Laves eutectics with no  $\eta$  phase formation is achieved after a PWSHT is performed at 1060 °C. Relative to INCONEL® alloy 718, the complete elimination of the  $\gamma$ /Laves eutectic constituents in the FZ of G27 through a PWSHT was proven to be achieved without causing excessive grain growth in the BM, which could be due to the pinning effect of the fine molybdenum (Mo)-rich precipitates, that are formed during solution heat treatment and identified as hexagonal close-packed phase particles through extensive (S)TEM analyses.

## 1. Introduction

G27 is a  $\gamma'$ -strengthened nickel-based superalloy intended for the aerospace industry that has been recently developed with mechanical properties comparable to those of Waspaloy in terms of stress rupture, high-temperature strength, notch ductility, stability, and resistance to crack growth under dwell fatigue [1]. This new alloy is intended and a promising material candidate for elevated-temperature applications such as the hot structural components of jet engines with a service temperature that can be as high as 760 °C. G27 is designed to be cobalt (Co)-free with a substantially lower raw material cost in comparison to Waspaloy.

Welding has been widely used to fabricate jet engines' hot structural components in the aerospace industry. It is believed that the fabrication of jet engines' hot sections by joining small pieces of superalloys through the welding process instead of casting a single large component offers several resultant benefits, such as enhanced flexibility in design, where, e.g. it becomes viable to join cast (geometrically complex) alloys with wrought (high strength) alloys or even join completely different

superalloys [2]. Another advantage is that the total weight of the parts is reduced, and the engine's fuel efficiency is enhanced, thus ultimately reducing environmental impact [2]. One of the most standard techniques used to fabricate the hot structural components of aero-engines is tungsten inert gas (TIG) welding. TIG welding techniques have undergone substantial advancements that have paved the way for the fabrication of these components and currently use faster travel speeds to allow for deeper penetration of welds. One of the most recent TIG welding techniques is keyhole TIG (K-TIG) welding, which enables welding at a faster travel speed to produce a full penetration weld in a single pass compared to conventional TIG welding, which cannot do so [4]. Furthermore, K-TIG welding is much easier to implement and more cost-effective than other high-energy density welding techniques, such as electron and laser beam welding processes [3], so, this technique is well-suited for on-site fabrication processes. The principles behind K-TIG welding have been explained in detail by Fei et al. [5].

The properties and reliability of the superalloy weldments are influenced by the microstructural development of the FZ during the rapid solidification of the weld. The FZ in superalloy welds typically

\* Corresponding author at: Department of Engineering Science, University West, SE-46186 Trollhättan, Sweden.

E-mail address: [achmad.ariaseta@hv.se](mailto:achmad.ariaseta@hv.se) (A. Ariaseta).

<https://doi.org/10.1016/j.matchar.2023.113178>

Received 6 June 2023; Received in revised form 30 June 2023; Accepted 11 July 2023

Available online 16 July 2023

1044-5803/© 2023 The Authors. Published by Elsevier Inc. This is an open access article under the CC BY license (<http://creativecommons.org/licenses/by/4.0/>).

consists of  $\gamma$  dendrites and microsegregation-induced secondary solidification microconstituents in the interdendritic regions. Microsegregation and non-equilibrium phase transformations during weld solidification can lead to the formation of unwanted intermetallic phases and chemical inhomogeneity in the FZ, which potentially negatively affect the properties and integrity of the welded component adversely. In some cases, the solidification microconstituents may also tie up the essential hardening elements, which could also cause other adverse effects on the elevated-temperature performance of the weld [6].

Post-weld solution heat treatments (PWSHTs) are usually carried out on most superalloy weldments to homogenize the as-welded microstructure, eliminate potentially harmful intermetallic phases, and relieve residual stresses to obtain optimum and reliable properties. The development of a suitable PWSHT largely depends on the as-welded FZ microstructure. In some cases, however, eliminating the harmful intermetallic microconstituents in the FZ of superalloy weld through PWSHT is challenging because the PWSHT may result in severe grain growth in the BM, which can deteriorate its mechanical properties. A well-known example is the widely used INCONEL® alloy 718, where completely removing brittle Laves eutectic constituents in the weld FZ through PWSHT leads to excessive grain growth in the BM, implying that such PWSHT is not feasible for INCONEL® alloy 718 weld joint [7,8]. Ram et al. [9] reported that the PWSHT performed to completely eliminate Laves phase induces severe grain growth in the BM of INCONEL® alloy 718, which ultimately results in deterioration of the tensile properties of the welded component due to the coarse grain in the BM region.

Therefore, in order to optimize the properties and integrity of G27 weldment by suitable PWSHT, a proper understanding of the as-welded FZ microstructure of G27 obtained after welding and PWSHTs and the grain growth behavior of the BM during PWSHT is paramount. However, since G27 is a new alloy, the secondary interdendritic microconstituents formed in the FZ during welding, especially K-TIG welding, have not yet been positively identified. Moreover, the response of the secondary interdendritic microconstituents to PWSHTs and the grain growth behavior in the BM during PWSHTs are still unknown. Thus, this work aims to study the FZ microstructure of G27 after K-TIG welding and PWSHTs and characterize the grain growth behavior of the BM during SHTs. The observed interdendritic microsegregation of different alloying elements and the formation of secondary solidification microconstituents in the interdendritic regions during the weld solidification of G27 are presented. Furthermore, the elimination of potentially deleterious interdendritic microconstituents after PWSHT and the grain growth behavior of the BM during SHT are also presented and discussed.

## 2. Experimental procedure

### 2.1. Keyhole TIG welding

As-received G27 alloy with dimensions of 300x30x4.2 mm in the as-hot-rolled plate condition with the chemical composition (in wt%) shown in Table 1 was used for the bead-on plate weld runs by using a K-TIG robotic welding process. The K-TIG welding operation was carried out with a welding current of 425 A, travel speed of 12 mm/s, and keeping a constant distance between the electrode tip and workpiece of 1.5 mm. High-purity argon gas (99.99%) was used as the shielding gas,

with a flow rate of 10 ml/min through a copper pipe. The welding parameters were chosen to create a full penetration weld in a single pass with a minimum weld width that is greater than 1.5 mm with minimum undercut and underfill, and little excess weld metal through the weld face and root. No evidence of cracking was found in the heat affected zone (HAZ) and FZ of any of the samples.

### 2.2. Post-weld solution heat treatment

The as-welded plates were excised into transverse sections at their center. PWSHTs were performed on the transverse sections at temperatures of 954, 982, 1010, 1040, and 1060 °C in a box furnace in an air atmosphere followed by water quenching.

### 2.3. Investigation on grain growth of BM

First, a pre-solution heat treatment (SHT) was performed on the as-received unwelded samples with dimensions of 5x30x4.2 mm in a box furnace in air atmosphere at 1030 °C for 300 s followed by water quenching. This pre-SHT was carried out because the as-received sample (Fig. 1a) has a severely deformed grain structure with unrecrystallized grains, which makes it difficult to accurately measure the grain size through optical microscopy (OM). The pre-SHT routine was carefully selected to fully recrystallize the grain structure while maintaining the relatively fine grain size before soaking the samples in SHT temperatures. After the pre-SHT, a fully recrystallized grain structure with a mean grain size of 19  $\mu\text{m}$  (Fig. 1b) was obtained with no  $\gamma'$  precipitates observed in the microstructure. Then, the pre-solution heat-treated samples were subjected to an SHT at temperatures between 954 and 1100 °C for 1 h to study the grain growth behavior. At 1060 °C, additional SHTs at different soaking times, i.e. 0.5 h, 2 h, and 4 h were carried out with a wrought INCONEL® alloy 718 used as a benchmark in addition to an SHT for 1 h. The INCONEL® alloy 718 used for the SHTs was in a solution-annealed condition, and its chemical composition is provided in Table 2. Note that for all of the samples, the temperature initially dropped by about 30–35 °C after they were inserted into the furnace. As a result, the SHT commenced once the furnace temperature reverted back to the target temperature. This was observed consistently to be within a period of 5 min. Grain size measurement was performed by using the Abrams three-circle procedure in accordance with ASTM E112 on at least five randomly selected OM images for each sample. The OM images were taken with a Zeiss Axio Imager M2m optical microscope.

### 2.4. Microstructural characterization

Transverse cross sections were cut from the center of an as-welded plate, and the transverse sections were subjected to PWSHTs. The mounted cross-sections were then prepared by multistep grinding with grit sizes down to 5  $\mu\text{m}$ , followed by polishing with a 3  $\mu\text{m}$  diamond suspension and 0.02  $\mu\text{m}$  of colloidal silicon dioxide ( $\text{SiO}_2$ ). Electrolytic etching was performed on the metallographic prepared samples using 10% oxalic acid at 2 V. The solution heat-treated samples were also cut, mounted, ground, and polished with the same standard metallographic procedure. A preliminary microstructural examination of the as-welded

**Table 1**  
Chemical composition of G27 in wt%.

Element	Ni	Al	Ti	Nb	S	Cr	Ta	V	Zr	Mo	Co
wt%	Bal.	1.90	1.88	3.70	0.001	15.11	<0.02	0.1	0.03	4.02	0.18
Element (cont.)	Si	Mn	C	P	Cu	Ca	Mg	B	N	O	Fe
wt% (cont.)	0.06	0.06	0.028	0.007	0.04	<0.0005	0.0034	0.005	0.006	0.001	15.00



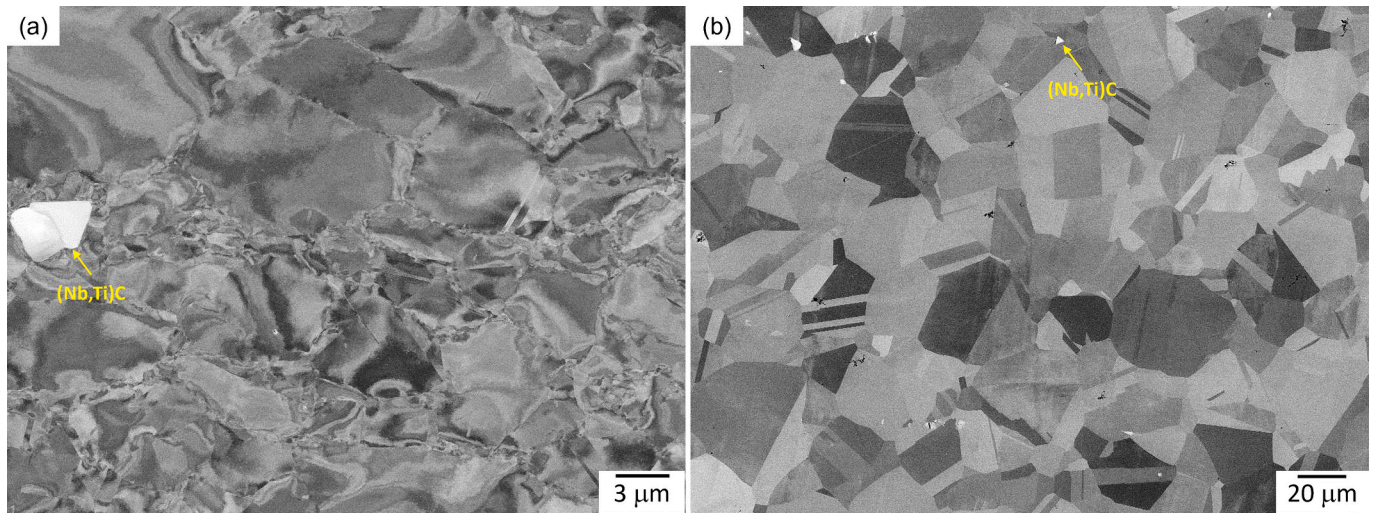


**Fig. 1.** SEM BSE images of (a) microstructure of as-received G27 which shows presence of unrecrystallized  $\gamma$  grains, and (b) pre-solution heat-treated sample which shows presence of fully recrystallized  $\gamma$  grains.

**Table 2**

Chemical composition of INCONEL® alloy 718 in wt% used in isothermal heat treatment.

Element	Ni	Al	Ti	Nb	S	Cr	Mo	Co
wt%	Bal.	0.38	1.04	5.18	0.0004	18.4	2.92	0.06

Element (cont.)	Si	Mn	C	P	Cu	B	Fe
wt% (cont.)	0.07	0.05	0.05	0.008	0.01	0.003	20.4

samples was carried out by OM. A more detailed microstructural investigation was performed by using a ZEISS Gemini field emission scanning electron microscope equipped with an Oxford AZtec energy-dispersive (EDS) detector and an FEI Talos F200X scanning transmission electron microscope equipped with a Super-X 4-quadrant EDS detector operated at 200 kV (at Manitoba Institute of Materials; University of Manitoba). The STEM images were taken by using a high-angle annular dark field (HAADF) detector. The TEM samples were prepared from the as-welded and heat-treated BM samples by mechanically grinding discs with a 3 mm diameter to a thickness of  $\sim 100$   $\mu\text{m}$ . Then, the discs were twin-jet electropolished in a solution of 8% perchloric acid in methanol at 243 K and 16 V.

## 2.5. Hardness testing

Vickers microhardness testing was performed on the BM, heat-affected zone (HAZ), and FZ of as-welded samples using a 0.5 kgf force (HV0.5) with a dwell time of 15 s. The measured values in the BM, HAZ, and FZ represent the average of seven indentations, with the corresponding standard deviation as a measure for the error.

## 2.6. Thermodynamic calculations

Thermo-Calc 2021b software was used for the non-equilibrium (Scheil) solidification and equilibrium phase diagram calculations with the TTNI8 database.

## 3. Results and discussion

### 3.1. Microstructure of fusion zone of as-welded G27

#### 3.1.1. Optical microscopy of as-welded microstructure of fusion zone

Fig. 2 shows the OM image of the as-welded microstructure of the FZ, which is a cellular dendritic microstructure. The average secondary dendrite arm spacing (SDAS),  $\lambda_s$ , in the FZ of the as-welded G27, is about  $6.9 \pm 0.8$   $\mu\text{m}$ , which was taken from the measurements close to the weld centerline. However, the SDAS measurement close to the fusion boundaries yielded an average value ( $7.0 \pm 0.7$   $\mu\text{m}$ ) comparable to the value obtained from the weld centerline, which suggests that the SDAS does not vary in size with different positions within the weld. Quested and McLean [10] reported that the SDAS is dependent on the cooling rate by using:

$$\lambda_s = k_s \theta^{-n} \quad (1)$$

where  $k_s$  and  $n$  are constants and their value depends on the alloy system, and  $\theta$  is the cooling rate. Using the values of  $k_s = 62.9$  and  $n = 0.407$ , as determined experimentally by Ling et al. [11] for a Ni-based superalloy, and substituting 6.9  $\mu\text{m}$  for  $\lambda_s$  in Eq. (1), the cooling rate within the FZ in G27 is calculated to be  $\sim 228$   $^{\circ}\text{C/s}$ . This cooling rate is

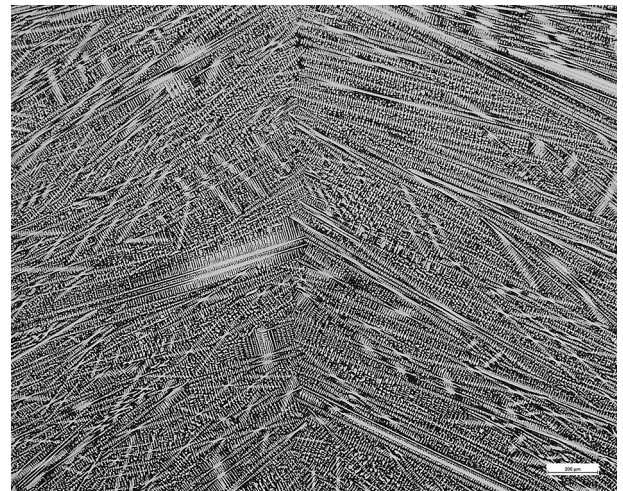


**Fig. 2.** OM image of FZ of as-welded G27.

significantly more rapid than that during conventional investment casting of alloy ingots, which is typically less than 5 °C/s.

### 3.1.2. Elemental partitioning in fusion zone of as-welded G27

The average chemical compositions of 30 points at the center of the dendrite core close to the fusion boundaries, as determined by using scanning electron microscopy-energy dispersive x-ray spectroscopy (SEM-EDS), are given in Table 3. An essential weld solidification parameter that can be determined from the data is the partition coefficient of the alloying elements,  $k$ , during the solidification of the weld FZ. As stated earlier, the estimated cooling rate within the FZ of G27 is approximately 228 °C/s. This rapid cooling rate would appreciably limit solute diffusion in the solid. Thus, there is the assumption that there is no diffusion in the solidified liquid during weld solidification. Dupont et al. [12] also reported that the substitutional element diffusion in austenite during weld solidification with fusion welding is negligible. Bower et al. [13] stated that by disregarding undercooling at the dendrite tips and assuming a complete mixing of the liquid without diffusion in the solid state materials under equilibrium conditions, the solute redistribution can be described by using the Scheil equation:

$$C_s = kC_0[1 - f_s]^{(k-1)} \quad (2)$$

where  $C_s$  is the composition of the solidified solid at the solid/liquid interface,  $C_0$  is the nominal composition of the alloy, and  $f_s$  is the fraction of the solidified solid. When the weld starts to solidify and  $f_s = 0$ , the first solid to form from the liquid, i.e. the dendrite core, will have a composition of  $kC_0$  under local equilibrium conditions and assuming negligible undercooling at the dendrite tips. Thus, the ratio between the chemical composition of the dendrite core and the nominal composition of the alloy will affect the initial partition coefficient at the start of weld solidification. The initial  $k$  values at the beginning of solidification of the major metallic alloying elements in G27, which include aluminum (Al), titanium (Ti), niobium (Nb), chromium (Cr), molybdenum (Mo), nickel (Ni), and iron (Fe), were obtained with an SEM-EDS analysis and are listed in Table 3.

Table 3 shows that Nb and Ti have  $k$  values considerably less than unity which indicates that these elements are strongly rejected into the interdendritic liquid during solidification. Molybdenum, Al, and Cr also segregated into the interdendritic regions but to a lesser extent than Nb and Ti. Nickel and Fe have  $k$  values  $>1$ , thus implying that they tend to selectively partition into the dendrite core. A comparison of the  $k$  values obtained in this work with those reported in the literature [14–16] on other Ni-based superalloys listed in Table 3 shows that the segregation behavior of Nb, Ti, Ni, Mo, and Fe is similar to that observed in other superalloys, where Nb, Mo and Ti segregate into the interdendritic region, whereas Ni and Fe partition into the dendrite core region.

Due to the difficulty of quantifying these light elements with adequate accuracy, the  $k$  values of carbon (C) and boron (B) cannot be determined in this study. In addition, the effect of back-diffusion of the interstitial elements can be substantial during weld solidification. However, Knorovsky et al. [17] suggested that the partition coefficient of C in alloys similar to INCONEL® alloy 625, a Ni-based superalloy, is

about 0.2. Thompson et al. [18] also reported on another Ni-based superalloy, INCONEL® alloy 718, and experimentally verified through Auger electron spectroscopy that C is rejected into the interdendritic liquid during solidification. The binary Ni–X phase diagram suggests that the  $k$  values for C and B in Ni are less than unity [13]. Thus, it is plausible that during the solidification of G27 welds, the C and B atoms extensively segregate into the interdendritic liquid. Other minor elements, such as silicon (Si) and zirconium (Zr), are excluded in Table 3. Our SEM-EDS analysis on Si and Zr resulted in  $k$  values of  $1.10 \pm 0.66$  and  $2.03 \pm 2.50$ , respectively. Such significant standard deviations for the  $k$  values of Si and Zr imply that the values are neither reliable nor conclusive in this work. This could be due to the limitations of the SEM-EDS analysis on quantifying elements with concentrations lower than 0.1 wt%. Note that the Si and Zr contents in the nominal alloy composition are 0.07 and 0.06 wt%, respectively. However, Paulonis et al. [14] reported that Si strongly segregates into the interdendritic region in INCONEL® alloy 718, with a  $k$  value of 0.67. As for Zr, Ojo et al. [16] reported that the  $k$  value of Zr is 0.13 in IN-738LC. Hence, it is also reasonable to presume that Si and Zr are strongly rejected into the interdendritic liquid during solidification. Nevertheless, the  $k$  values are not necessarily constant during the solidification process. Still, they may explain well the formation of secondary interdendritic microconstituents, as discussed in the next section.

### 3.1.3. Secondary solidification microconstituents in the fusion zone of as-welded G27

An SEM-EDS analysis conducted at high magnification (Fig. 3) revealed the discrete distribution of some secondary phase microconstituents along the interdendritic regions of the FZ of the as-welded alloy. The first particle has an irregular shape and wavy interface, whereas the second particle has blocky and rod-like morphologies. Their morphologies and Nb-rich character, as found in our preliminary SEM-EDS analysis [19] suggest that they are Laves phase and MC-type carbides.

(S)TEM analyses were carried out to positively identify the secondary interdendritic microconstituents in the FZ. Fig. 4 depicts a STEM HAADF image with the corresponding selected area diffraction patterns (SADPs) of blocky-shaped interdendritic microconstituents. Details of the STEM-EDS microchemical analysis are presented in Table 4. The table shows that the particles have a high Nb content with a relatively substantial amount of Ti and Mo. The SADPs of the [110], [211], and [321] zone axes shown in Fig. 4(b)–(d), respectively, suggest that the crystal structure of the particles is a cubic NaCl structure with a lattice parameter of  $a = 0.44$  nm. It can be concluded from the STEM-EDS analysis and SADPs that these particles are MC-type carbides

**Table 3**

Chemical composition of dendrite core (wt%) and calculated partition coefficients of major alloying elements,  $k$ .

Element	Al	Ti	Cr	Fe	Ni	Nb	Mo
wt%	1.57	1.05	14.28	15.35	62.88	1.54	3.20
$k$ , G27	0.82	0.56	0.94	1.02	1.08	0.42	0.80
Standard deviation of $k$ , G27	0.03	0.07	0.02	0.03	0.02	0.05	0.04
$k$ , INCONEL® alloy 718 [14]	1.00	0.63	1.03	1.04	1.00	0.48	0.82
$k$ , ATI 718Plus [15]	1.10	0.70	1.10	1.10	1.00	0.50	0.90
$k$ , IN 738 LC [16]	0.92	0.69	0.98	–	1.03	0.58	–

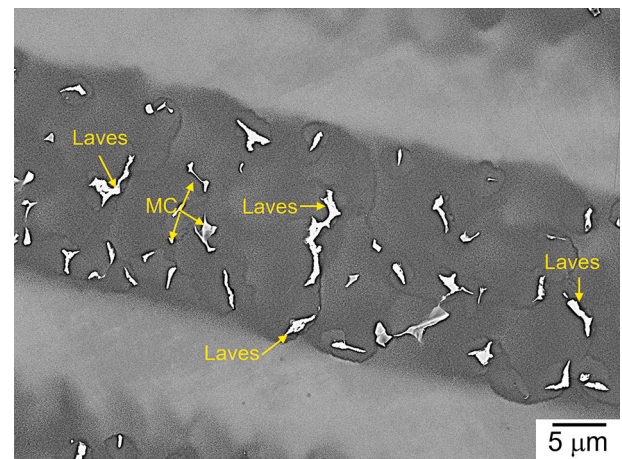


**Fig. 3.** SEM-BSE micrograph of an interdendritic region of FZ of as-welded G27.



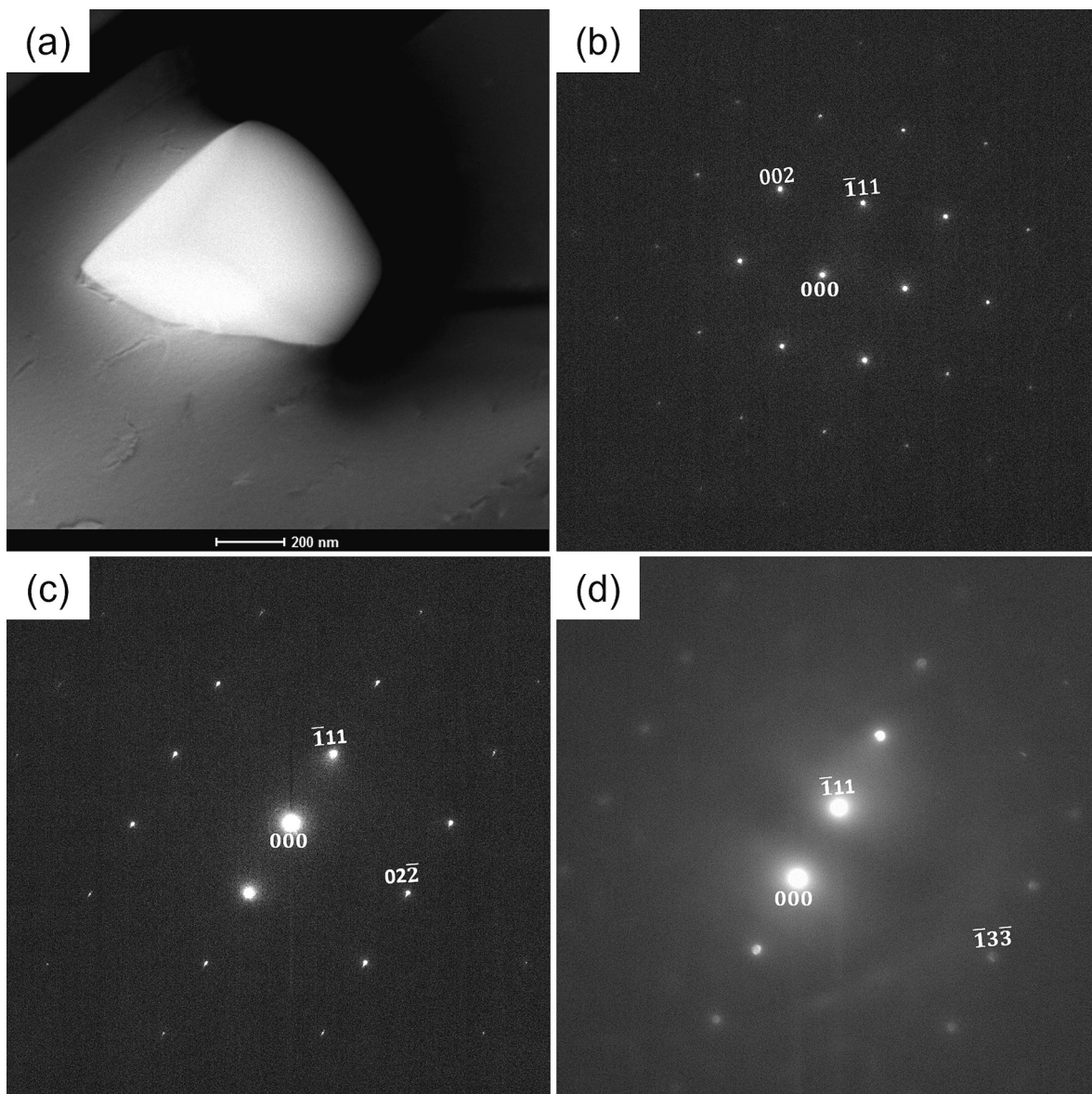


**Fig. 4.** TEM analysis of FZ of as-welded G27 that shows: (a) HAADF image of Nb-rich MC carbide, and SADPs of (b) [110], (c) [211], and (d) [321] zone axes of MC carbide.

**Table 4**  
STEM-EDS analysis of Laves phase and MC carbide in wt% and at%.

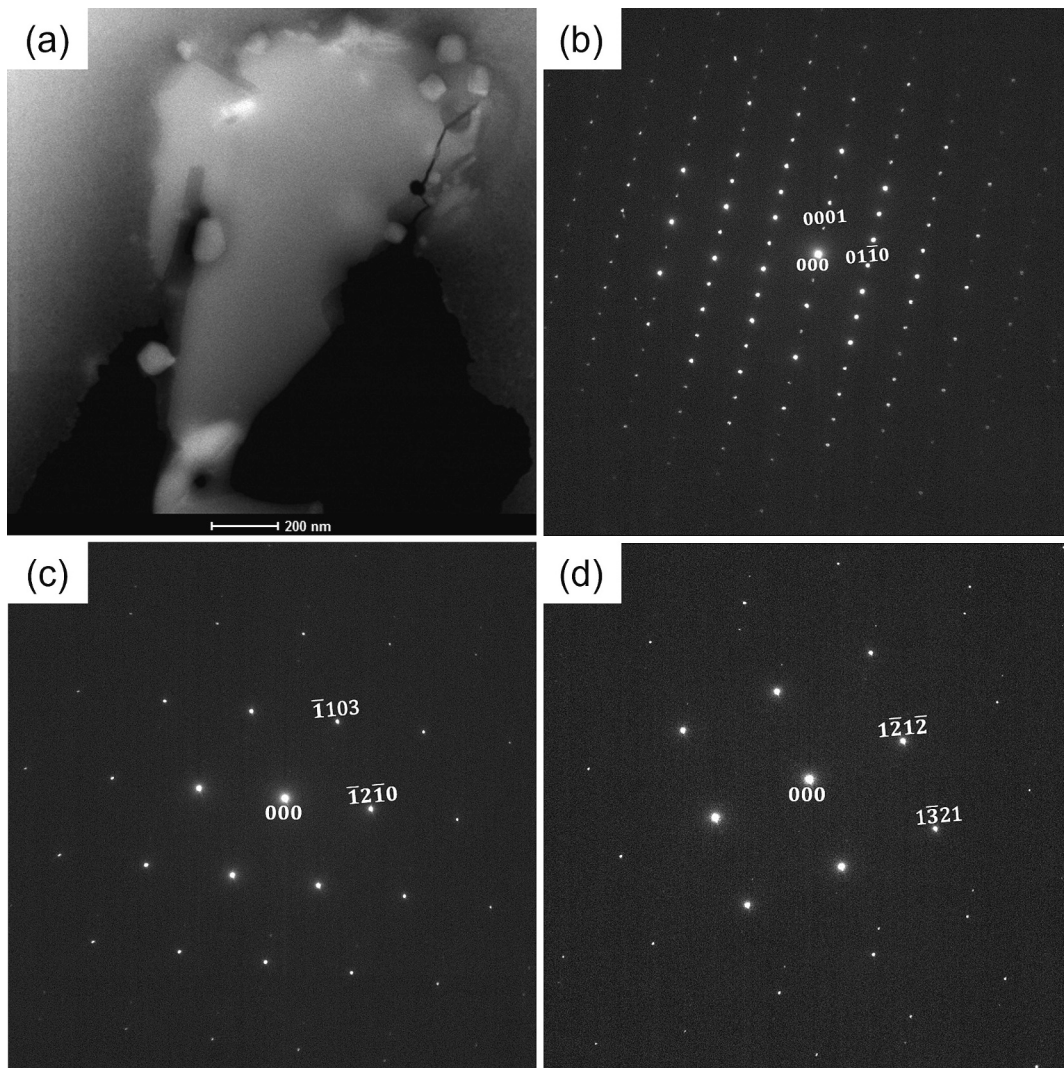
Element	Laves phase		MC carbide	
	wt%	at%	wt%	at%
Al	0.63	1.49	0.22	0.67
Si	2.39	5.46	–	–
Ti	1.99	2.66	12.05	20.60
Cr	11.42	14.07	1.05	1.65
Fe	9.59	11.01	0.38	0.56
Ni	36.10	39.41	0.97	1.35
Zr	2.06	1.45	–	–
Nb	24.27	16.74	75.48	66.51
Mo	11.55	7.72	9.28	7.91
Cu	–	–	0.57	0.74

composed of Nb as the main metallic element and Ti and Mo as a secondary metallic element, i.e., (Nb, Ti, Mo)C. Likewise, a STEM HAADF image of the irregular-shaped interdendritic microconstituents and the corresponding SADPs of the  $[2\bar{1}10]$ ,  $[30\bar{3}1]$ , and  $[32\bar{1}13]$  zone axes are

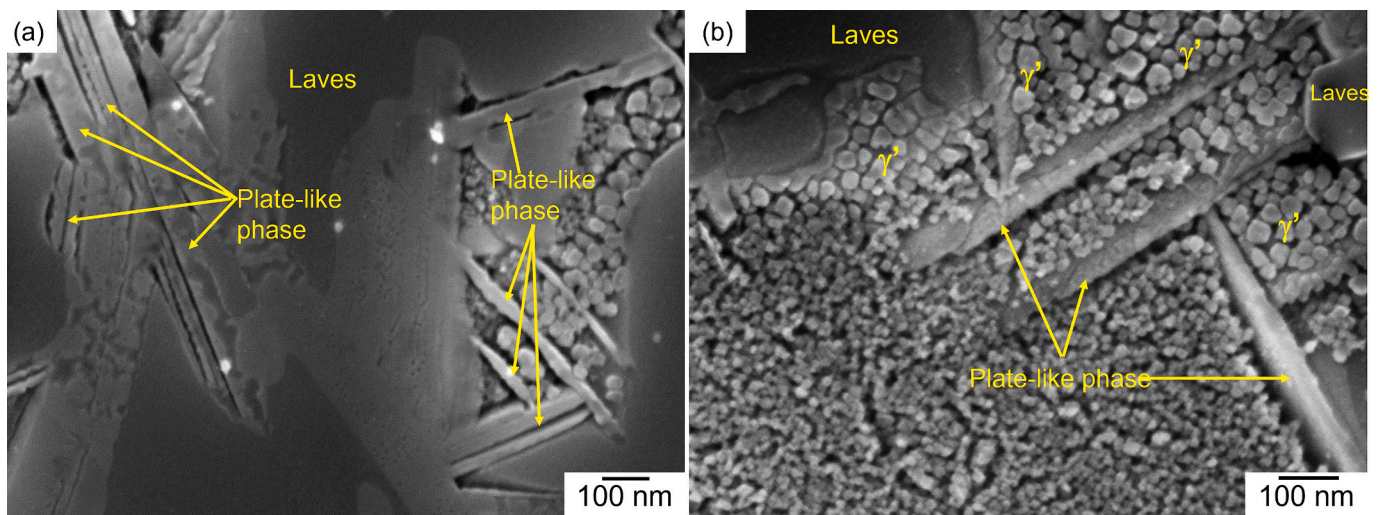
shown in Fig. 5. The STEM-EDS analysis results show that these particles contain a relatively high amount of Nb, Mo, Ni, Fe, and Cr and some other minor elements such as Si and Zr that exhibit a composition close to  $(\text{Ni, Cr, Fe})_2(\text{Nb, Mo, Ti, Si, Zr})$  as summarized in Table 4. The presence of Si and Zr in the Laves phase also confirms that both elements segregate into the interdendritic liquid during solidification. Also, the SADPs in Fig. 4(b)–(d) reveal that these particles have a hexagonal close-packed crystal structure with lattice parameters of  $a = 4.73 \text{ \AA}$  and  $c = 7.86 \text{ \AA}$ . The crystal structure and lattice parameters obtained from the SADPs along with the chemical composition of the microconstituents confirm that the irregular-shaped particles are the Laves phase.

Fig. 6(a) shows a high magnification SEM in-lens image of the Laves eutectic constituent in the interdendritic region of the as-welded sample, thus revealing the presence of plate-like phase particles. The morphology of these particles indicates that they could be either the  $\eta$  or  $\delta$  phase, as frequently reported in the grain boundaries of ATI 718Plus and 718 superalloys, respectively. (S)TEM analyses were then carried out to identify the plate-like phase. A TEM-bright field (BF) image of the plate-like phase particle (Fig. 7a) and the corresponding SADPs of the particles in the FZ of the as-welded sample by using the zone axes





**Fig. 5.** TEM analysis of FZ of as-welded G27 that shows: (a) HAADF image of Laves phase particle, and SADPs of (b)  $[2\bar{1}\bar{1}0]$ , (c)  $[30\bar{3}1]$ , and (d)  $[3\bar{2}\bar{1}\bar{3}]$  zone axes of Laves phase.



**Fig. 6.** (a) SEM-BSE image that shows presence of plate-like phase close to Laves eutectic constituent in the interdendritic region of the FZ, (b) higher magnification SEM in-lens image of area marked yellow to (a) show presence of plate-like phase and  $\gamma'$  immediately adjacent to the Laves particle. (For interpretation of the references to colour in this figure legend, the reader is referred to the web version of this article.)



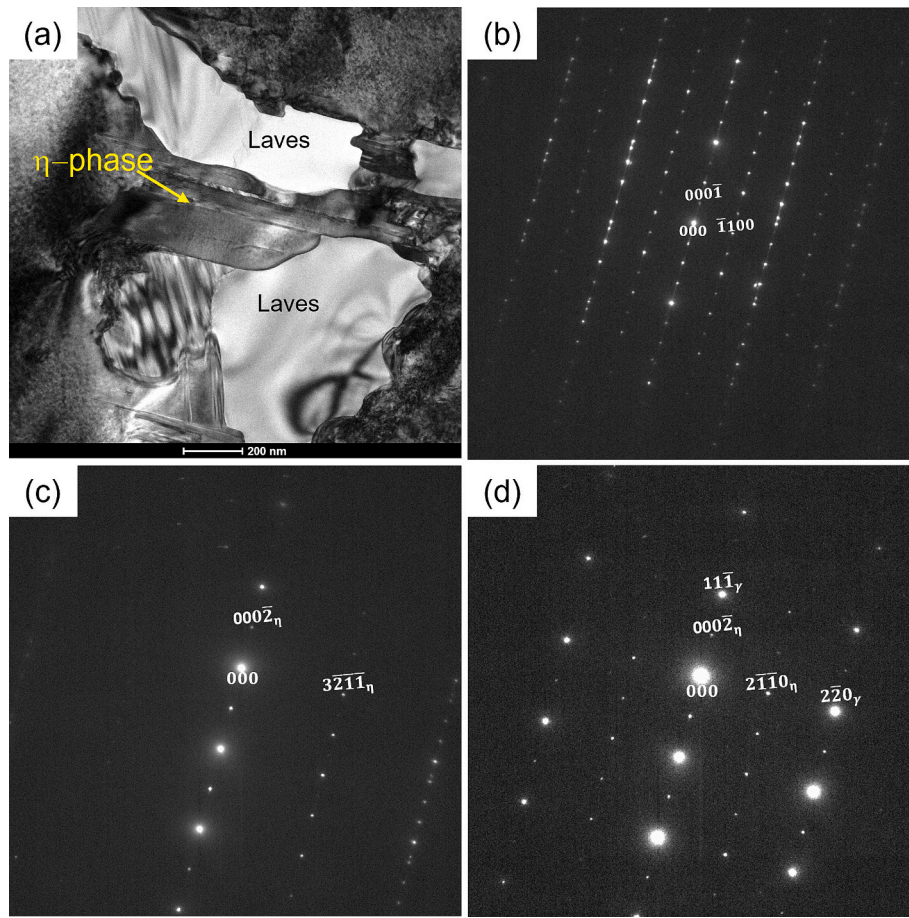


**Fig. 7.** TEM analysis of FZ of as-welded G27 that shows: (a) BF image of  $\eta$  phase particle, and SADPs of (b)  $[14\bar{5}0]_{\eta}$ , (c)  $[\bar{1}\bar{1}20]_{\eta}$ , and (d)  $[112]_{\gamma}$  ( $[01\bar{1}0]_{\eta}$ ) zone axes.

parallel to  $[14\bar{5}0]_{\eta}$ ,  $[\bar{1}\bar{1}20]_{\eta}$ , and  $[112]_{\gamma}$  ( $[01\bar{1}0]_{\eta}$ ) are shown in Fig. 7 (b)-(d), respectively. The SADPs reveal that the structure of the plate-like phase is consistent with the  $\eta$ -ordered hexagonal close-packed ( $\text{DO}_{24}$ ) structure reported by Pickering et al. [20] in the grain boundaries of ATI 718Plus. Furthermore, the SADPs in Fig. 7(b)-(d) reveal that the plate-like phase has approximate lattice parameters of  $a = 5.07 \text{ \AA}$  and  $c = 8.45 \text{ \AA}$ . These values are very close to those reported in Pickering et al. [20] for the  $\eta$  phase in ATI 718Plus and in Laves and Wallbaum [21] for  $\eta\text{-Ni}_3\text{Ti}$ . In addition, the STEM-EDS point analysis in Table 5 shows the chemical composition of the plate-like phase particles. The phase is enriched in Ni, Nb, Ti, and some Al. These four elements are also the main components of the  $\eta\text{-Ni}_3\text{Ti}$  phase reported in ATI 718Plus [20]. However, the Cr and Fe contents of the  $\eta\text{-Ni}_3\text{Ti}$  phase particles in the FZ of the as-welded G27 are higher than those of the  $\eta$  phase in ATI 718plus in Pickering et al. [20]. From the TEM SADPs and STEM-EDS analysis, the plate-like phase formed close to the Laves phase along the interdendritic region of the FZ of the as-welded G27 is likely a hexagonal close-packed  $\eta$  phase.

Apart from the  $\eta$  phase, the presence of  $\gamma'$  particles in the matrix near the Laves phase particles is also observed (Figs. 6(b) and 8(a)), as confirmed by the SADP (Fig. 8(b)), which shows the presence of superlattice reflections from the  $\gamma'$  precipitates in the matrix near the Laves phase. The spherical morphology of the  $\gamma'$  particles suggests that they likely formed through the solid-state precipitation during cooling.

**Table 5**  
STEM-EDS analysis of plate-like phase in FZ of as-welded sample (at%).

Element	Ni	Al	Ti	Nb	Mo	Cr	Fe
at%	67.79	3.80	8.18	6.01	1.20	6.45	6.58

The  $\gamma'$  phase formed as a solidification product, i.e.,  $\gamma\text{-}\gamma'$  eutectics, typically exhibits an irregular shape, as Ojo et al. [16] reported for the IN-738LC superalloy. It is shown in the SEM image in Fig. 6(b) that  $\gamma'$  cannot be resolved when it is further away from the Laves phase. This can be attributed to the microsegregation of Al and Ti in the interdendritic region, as their  $k$  values are 0.82 and 0.54, respectively. The matrix closest to the Laves eutectic is expected to be the richest in Al and Ti compared to that further away from the Laves eutectic. In addition, Nb segregation may also further accelerate the  $\gamma'$  precipitation kinetics, as reported in Asala et al. [15] in the FZ of ATI 718Plus. Therefore,  $\gamma'$  particles nucleate faster in the region closest to the Laves phase during cooling and have more time to grow due to enrichment of Al, Ti, and Nb. This may explain why  $\gamma'$  particles close to Laves particles are relatively coarser compared to those that are further away.

The unambiguous identification of secondary interdendritic microconstituents in the FZ of as-welded G27 through (S)TEM analyses in the present work also sheds light on the identification of the microconstituents observed in the HAZ close to the fusion boundary that consists of a partially melted zone (PMZ) with numerous liquated and resolidified regions grain boundaries, as reported in our previous study [19]. This region is frequently identified as the weakest area of the weldment [22]. In the HAZ close to the fusion boundary, we observed Nb-rich irregular-shaped particles, plate-like precipitates, Nb-rich blocky particles, and  $\gamma'$  precipitates present in the liquated and resolidified regions through our preliminary SEM-EDS analysis [19]. Based on the (S)TEM analyses on the microconstituents in the FZ in the present work, it implies that the microconstituents observed in the liquated and resolidified areas in the HAZ are irregular-shaped Laves eutectics, Nb-rich MC-type carbides,  $\eta$  phase and  $\gamma'$ . The details of the HAZ microstructure and a more comprehensive discussion have been presented

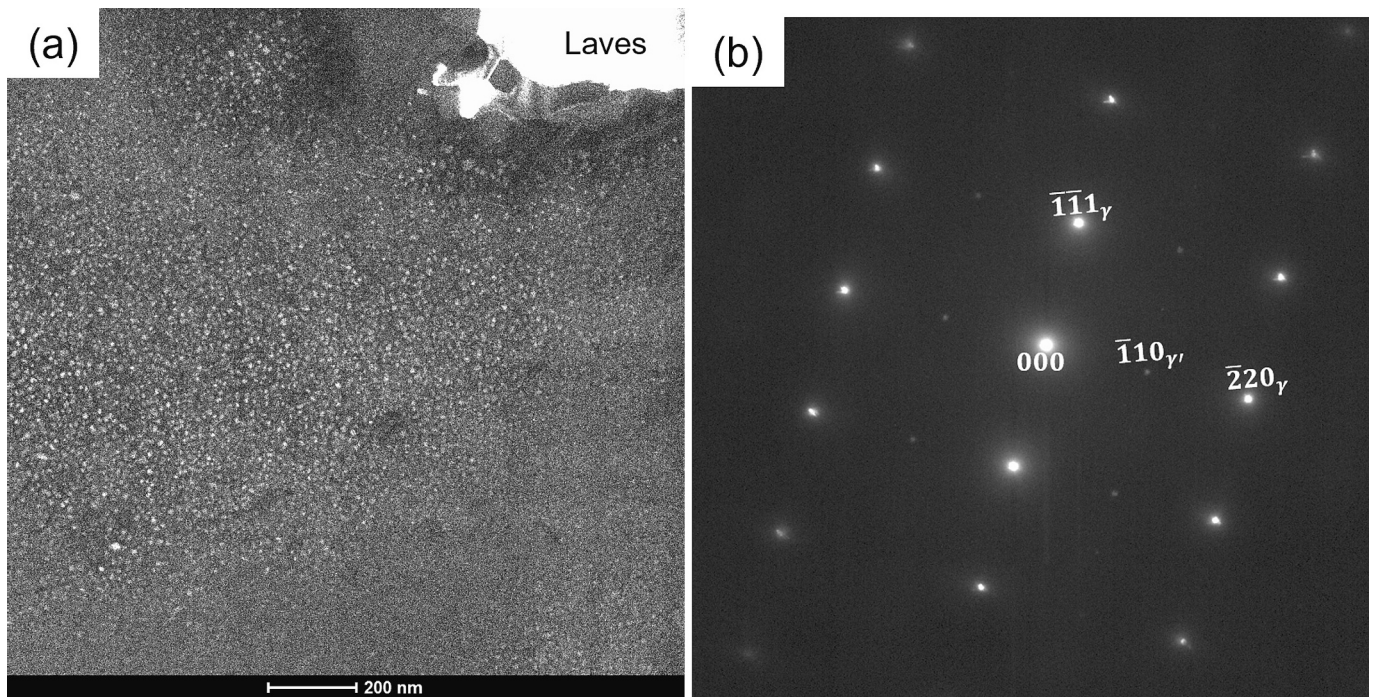


Fig. 8. (a) TEM-darkfield (DF) image that shows presence of  $\gamma'$  close to Laves phase, (b) STEM SADP of [112] zone axis that shows superlattice reflections from  $\gamma'$  taken from matrix close to the Laves phase in the interdendritic region.

elsewhere in our previous work [19].

#### 3.1.4. Hardness measurement on the as-welded G27

Fig. 9 shows the BM, HAZ, and FZ average Vickers microhardness values of the as-welded G27. The BM exhibited the highest average microhardness ( $502 \pm 6$  HV) due to its heavily deformed state (see again Fig. 1(a)) and the presence of  $\gamma'$  precipitates distributed uniformly throughout the microstructure, as seen in Fig. 10(a). In the HAZ, the average microhardness significantly dropped to  $382 \pm 5$  HV. This can be attributed to the dissolution of  $\gamma'$  precipitates due to heating during the welding thermal cycle. Fig. 10(b) shows the high-magnification SEM in-lens image that displays fine particles that appear to be  $\gamma'$  much finer than those of the BM, suggesting that  $\gamma'$  precipitates dissolve during the heating and reprecipitate during the weld cooling cycle. It was likely that the amount of tiny reprecipitated  $\gamma'$  was lower than that of the BM, resulting in less hardening in the HAZ compared to the BM. In addition,

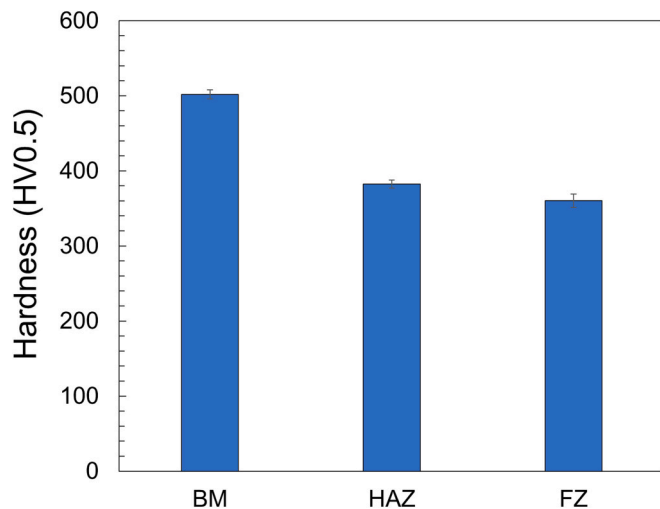


Fig. 9. Average microhardness values of BM, HAZ, and FZ of as-welded G27.

recrystallization occurs in the HAZ (Fig. 10(c)), which can also give a softening effect. The FZ possessed the lowest Vickers microhardness value among all regions ( $360 \pm 9$  HV). This could be explained by the fact that  $\gamma'$  particles did not form uniformly in the FZ, where they were mainly formed close to the Laves phase in the interdendritic region (see again Figs. 6(b) and 8(a)), whereas no evidence of  $\gamma'$  particles were observed in the dendrite core [19]. The softer dendrite core may result in relatively lower FZ average microhardness than the HAZ and BM.

#### 3.1.5. Microstructural development in the fusion zone during weld solidification

In order to understand the changes in the microstructure during the solidification of a weld, it is worth mentioning that G27 in this study contains 3.7 wt% Nb in its nominal composition. The Nb content is almost identical to that of INCONEL® alloy 625 [23], a commercial alloy that is considered to be one of the Nb-bearing Ni-based superalloys [24]. In such superalloys, for instance, INCONEL® alloys 625 and 718 and ATI 718Plus, Nb-rich phases such as MC carbides and Laves phases in the interdendritic region are generally well-known to form through eutectic reactions during solidification as a result of elemental microsegregation [15,17,22,24,25]. Thus, it is reasonable to assume that the formation of MC carbides and Laves eutectic particles in the interdendritic region of the FZ of G27 may follow a similar solidification pathway as those reported in other Nb-bearing superalloys.

DuPont et al. [24] reported that a solidification pathway in Nb-bearing Ni-based superalloys with a high Nb concentration ( $>2$  wt%) and low C concentration ( $<0.075$  wt%) can be generally described by using a three-step process [24]. Recall that the C concentration in G27 is 0.028 wt%; therefore, the Nb and C concentrations are within the ranges in DuPont et al. [24]. First, the solidification is initiated by the formation of primary  $\gamma$  dendrites through the reaction of  $L \rightarrow \gamma$ . During the growth of the dendrite, solute elements with  $k$  values less than unity are rejected into the interdendritic liquid. Once the solubility limit of these solute elements in the interdendritic liquid is exceeded, the secondary solidification microconstituents start to form from the liquid. During the growth of the primary  $\gamma$  dendrites, elements that tend to form MC carbides, i.e., Nb, Ti, Mo, and C, continuously enrich the interdendritic



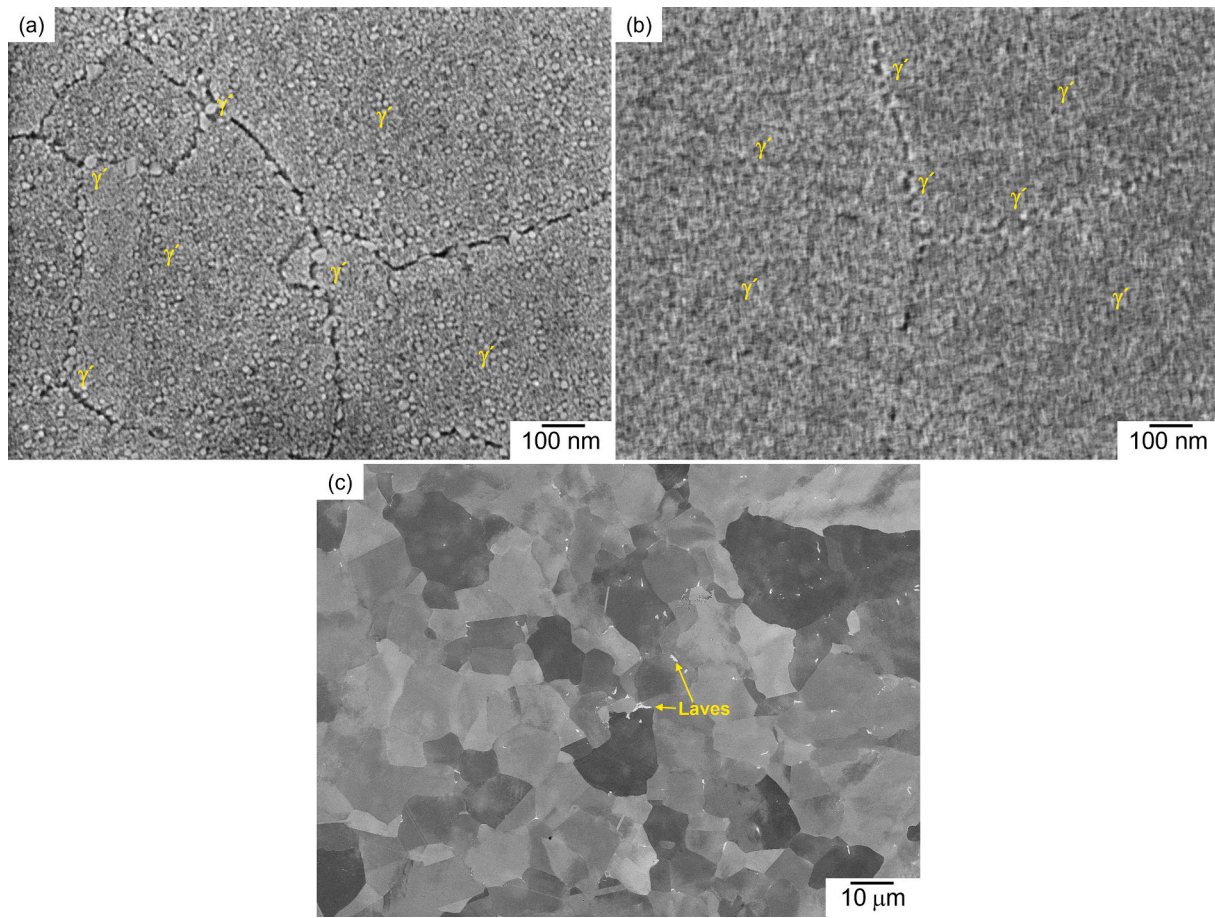


**Fig. 10.** (a) High magnification SEM in-lens image of BM, (b) high magnification SEM in-lens image of HAZ, (c) low magnification SEM BSE image of HAZ that shows recrystallized grains.

liquid, which could ultimately lead to the formation of MC-type carbides. This is most likely to take place through a monovariant eutectic reaction of  $L \rightarrow \gamma + MC$  over a temperature range. The formation of MC carbides from the liquid would deplete most available carbon from the interdendritic liquid. Then, during further cooling, the residual interdendritic liquid would continue to be enriched with Nb, which may eventually lead to the Laves phase formation through an  $L \rightarrow \gamma + \text{Laves}$  reaction over a range of temperatures as a result of the supersaturation of Nb. It is still unclear whether the  $\eta$  phase is formed via solidification or a solid-state precipitation reaction. Therefore, a Scheil solidification simulation was performed to predict the solidification products, as presented in Fig. 11. In the simulation, only phases experimentally observed in the microstructure were included, with the exclusion of  $\gamma'$  since it is thought to be formed via solid-state precipitation during cooling. The figure shows that the MC carbides and Laves eutectic constituents form over a range of temperatures with the reaction sequence in good agreement with the explanation above in DuPont et al. [24]. At the end of the solidification, it is predicted by using the Scheil simulation that the  $\eta$  phase is formed via a eutectic reaction. Therefore, it is possible that the  $\eta$  phase could be formed as a solidification product as it is theoretically predicted by using thermodynamic simulation. In addition, the  $\eta$  phase particles also appear to be associated and intermixed with the Laves phase (see Fig. 6(a)), which further support the theoretical calculation by Thermo-Calc that the  $\eta$  phase is likely formed from the liquid.

The presence of the Laves phase in the FZ of the as-welded G27 requires careful consideration since it is generally known that this phase in Ni-based superalloys has detrimental effects on the mechanical properties of the alloys. Schirra et al. [26] found that the Laves phase in

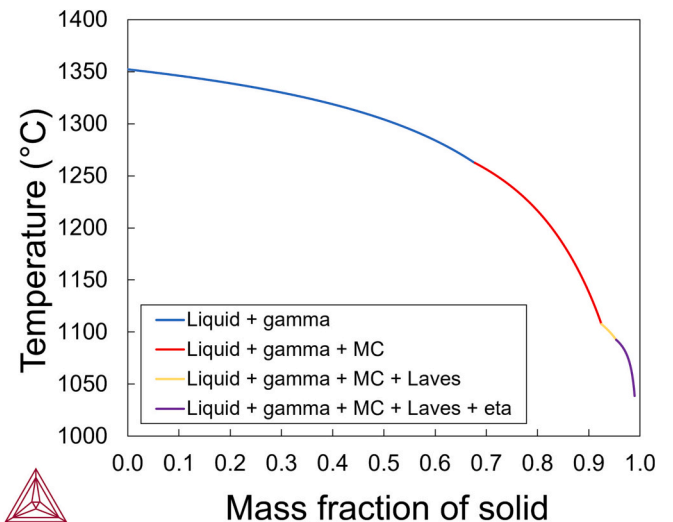


**Fig. 11.** Scheil solidification simulation by Thermo-Calc using a nominal alloy composition of G27.

INCONEL® alloy 718 has a weak interface with the  $\gamma$  matrix, thus easily acting as a preferential site for crack initiation and growth owing to its inherent brittle nature [27]. James [27] similarly reported that the weldment of INCONEL® alloy 718, which still contains a large amount of the Laves phase, exhibits a higher rate of crack growth at elevated temperatures than the weldment with a fully dissolved Laves phase.



Therefore, this work has shown that developing a suitable PWSHT is needed to eliminate or reduce the Laves phase in the weld FZ of G27 to optimize the weldment properties.

### 3.2. Post-weld solution heat-treated microstructure

Fig. 12(a-d) shows the microstructure of the FZ after undergoing a PWSHT for 1 h. Coarse irregularly-shaped Laves phase particles can still be observed and are only partially removed at temperatures up to 1010 °C (Fig. 12(a) and (b)). However, after the PWSHT at 1040 °C (Fig. 12(c)), irregular Laves eutectics were not observed, with most of the blocky particles observed being MC carbides, which suggests that the Laves phase particles were largely eliminated. Our SEM-EDS analysis conducted on fine particles near the MC carbides subjected to a PWSHT at 1040 °C revealed that they appear to be the few remaining Laves particles. The complete dissolution of the Laves eutectic constituents was achieved after a PWSHT was implemented at 1060 °C (Fig. 12(d)). The Laves eutectics in the HAZ close to the fusion boundary, i.e. PMZ, were also completely dissolved after PWSHT was carried out at 1060 °C. This study finds that the dissolution temperature of the Laves eutectic particles in the FZ of G27 ranges between 1040 and 1060 °C, which is in agreement with the dissolution temperature of the Laves phase in the FZ of TIG-welded ATI 718Plus in Asala et al. [15], where the complete elimination of the Laves phase occurs after a PWSHT at 1050 °C.

Fig. 12(a) and (b) also reveal that there is a significant formation of plate-like phase particles that surround the Laves phase after PWSHTs are implemented at temperatures from 954 to 1010 °C. The Laves phase appears to provide a favourable site for the plate-like phase formation (Fig. 13), which may explain why they are formed mainly around the Laves particles. Similar findings are reported in the literature where the

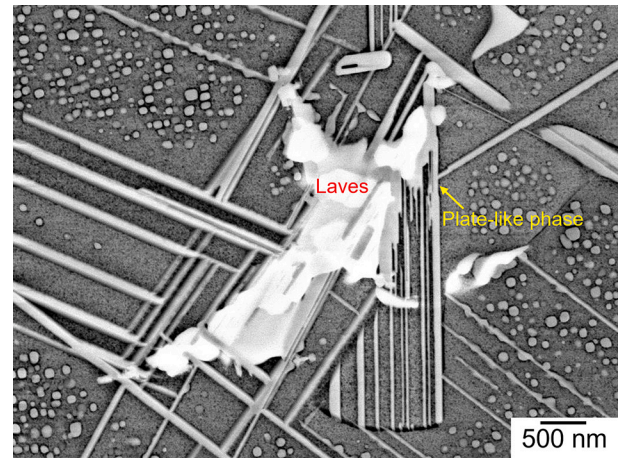


Fig. 13. SEM-BSE image that shows Laves eutectic particles are a favourable formation site for plate-like phase.

excessive formation of  $\delta$  and  $\eta$  platelets around the Laves particles occurs during a PWSHT between 954 and 982 °C in the FZ of INCONEL® alloy 718 [9] and ATI 718Plus [15], respectively. A large number of plate-like phase particles also needs warrant attention when choosing the most appropriate PWSHT since this may significantly impact the mechanical properties of the alloy. Researchers have reported that a large number of plate-like phases, such as the  $\delta$  phase in INCONEL® alloy 718 [28] and the  $\eta$  phase in ATI 718Plus [29], can be detrimental to the mechanical properties of the alloy. The formation of these phases is greatly reduced after a PWSHT is carried out at 1040 °C (Fig. 12(c)), and eventually, very

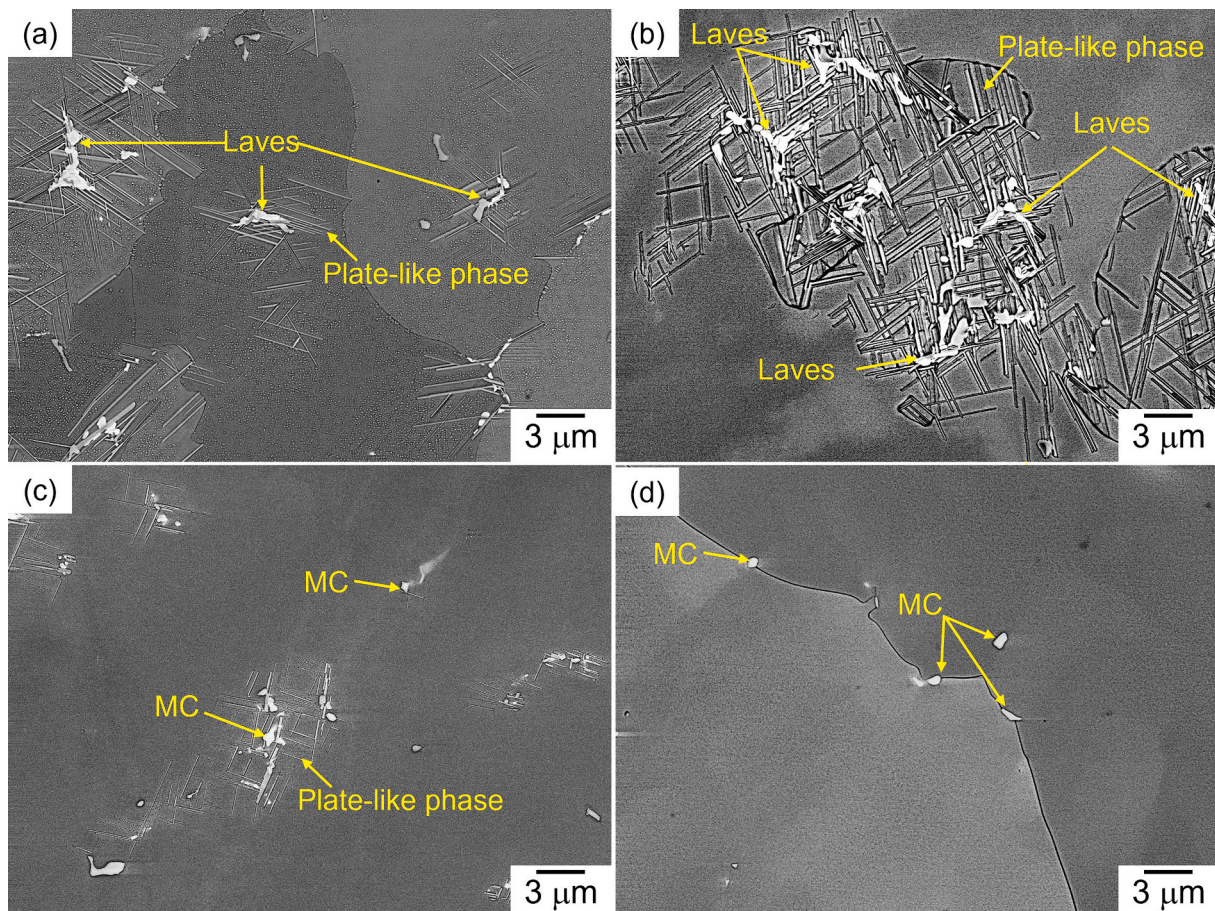


Fig. 12. SEM-BSE micrographs of FZ microstructure after PWSHT at (a) 954 °C, (b) 1010 °C, (c) 1040 °C, and (d) 1060 °C for 1 h.



minimal after a PWSHT at 1060 °C (Fig. 12(d)).

The presence of plate-like phase particles is also observed in the BM of samples that are post-weld solution heat-treated at temperatures between 954 °C and 1010 °C. An SEM-EDS analysis was performed on at least ten plate-like particles in the FZ and BM; the results are presented in Table 6. It can be observed that the chemical compositions of the plate-like particles in the FZ and BM based on the SEM-EDS are comparable, which suggests that they are the same type of particles. Fig. 14 (a) shows the TEM BF image and the corresponding SADPs of the plate-like phase in the BM of the post-weld solution heat-treated sample by using the zone axes parallel to  $[112]_{\eta}$  ( $[11\bar{4}76]_{\eta}$ ) and  $[001]_{\eta}$  ( $[30\bar{3}2]_{\eta}$ ), as shown in Fig. 14(b) and (c), respectively. The SADPs reveal that the plate-like phase has a  $\eta$ -ordered hexagonal close-packed ( $\text{DO}_{24}$ ) crystal structure with lattice parameters of  $a = 5.07 \text{ \AA}$  and  $c = 8.45 \text{ \AA}$ , which is identical to that of the  $\eta$  phase in the FZ of the as-welded sample. In addition, the STEM-EDS analysis performed on the plate-like phase (Table 7) also shows that the particles contain Ni, Al, Ti, and Nb, which are the primary  $\eta$  phase forming elements in ATI 718Plus, as reported in Pickering et al. [20]. Therefore, this implies that the plate-like phase formed in the FZ and BM in the post-weld solution heat-treated samples are believed to be hexagonal close-packed  $\eta$   $\text{Ni}_3\text{Ti}$  phase particles.

### 3.3. Grain growth behavior of base material during solution heat treatment

#### 3.3.1. Effect of solution heat treatment temperature on grain growth

The change in the grain size of the BM with SHT temperature is shown in Fig. 15, where the grain size remains unchanged after an SHT up to 1010 °C. Interestingly, a sharp increase in grain size from 19 to 37  $\mu\text{m}$  occurs at 1020 °C. Fig. 16(a) and (b) show the SEM BSE micrographs of samples that are solution heat-treated at 1010 °C and 1020 °C, respectively, observed on as-polished surfaces. It is found that the grain boundaries of the sample that has been solution heat-treated at 1010 °C are decorated by a high density of  $\gamma'$  precipitates that are imaged in dark contrast. Conversely, no trace of the  $\gamma'$  particles can be observed after the ST at 1020 °C, thus indicating that the  $\gamma'$  solvus temperature lies between 1010 and 1020 °C, which is in agreement with the equilibrium phase diagram calculation by Thermo-Calc as shown by the red line in Fig. 15. Apart from the  $\gamma'$  precipitates, other precipitates are found on the grain boundaries, which include coarse (Nb, Ti)C,  $\eta$  phase (Fig. 16 (c)), and bright precipitates (Fig. 16(a) and (b)). An SEM-EDS analysis showed that the bright precipitates are rich in Mo. However, the density of these precipitates appears to be much lower than that of the  $\gamma'$  precipitates. This means that, arguably, these particles do not significantly contribute to preserving the fine grain size during ST up to 1010 °C. Therefore, the  $\gamma'$  particles are likely to be responsible for controlling the grain size in the BM of G27 up to a temperature of 1010 °C by pinning the grain boundaries, and their dissolution is responsible for the extensive grain growth at 1020 °C. The role of the  $\gamma'$  precipitates in inhibiting grain growth during subsolvus ST was reported in Collins et al. [30] for a polycrystalline Ni-based superalloy, RR1000. Song et al. [31] also demonstrated that the  $\gamma'$  precipitates pin the grain boundaries and significantly inhibit grain growth in the subsolvus ST condition on a Ni-based superalloy.

In the absence of  $\gamma'$  precipitates, normal grain growth with temperature occurred at an almost constant rate between 1020 and 1080 °C

from 37 to 71  $\mu\text{m}$  (see again Fig. 15). This suggests that another mechanism governs the normal grain growth at this temperature range. Then, an increase in the SHT temperature from 1080 °C to 1100 °C resulted in another sharp increase in grain size from 71 to 114  $\mu\text{m}$ . Fig. 17(a) to (d) shows the SEM-BSE images of the samples solution heat treated at 1020–1100 °C. It is shown that two types of particles that pin the grain boundaries between 1020 and 1080 °C are coarse (Nb, Ti)C and fine Mo-rich precipitates. At 1100 °C, the Mo-rich precipitates are placed into the solution, thus resulting in the (Nb, Ti)C particles being the primary particles that pin the migrating grain boundaries during SHT at this temperature. This suggests that Mo-rich precipitates may be responsible for inhibiting grain growth between 1020 and 1080 °C.

Dispersion of randomly distributed second-phase particles is known to retard grain growth through the Zener pinning mechanism, where the Zener pinning pressure is expressed as [32]:

$$P_z = \frac{3V_f\gamma}{2r} \quad (3)$$

where  $P_z$  is the Zener pinning pressure,  $V_f$  is the volume fraction of the particles (often approximated by the area fraction),  $\gamma$  is the grain boundary energy, and  $r$  is the particle radius. Table 8 shows the average values of the area fraction ( $c$ ),  $r$  for MC carbides obtained from SHTs at 1080 °C and 1100 °C and the  $P_z$  is calculated by using the experimentally obtained average  $A_f$  and  $r$  and a value of  $0.8 \text{ J/m}^2$  used for  $\gamma$  used for Ni-based superalloy [33]. The average values of  $A_f$  and  $r$  were obtained by using ImageJ software on at least 25 OM images with a magnification that minimizes the number of individual measurements while still providing a clear image of the MC carbide. Trials were made to measure  $A_f$  and  $r$  for Mo-rich precipitates using ImageJ on SEM images with a magnification that minimizes the number of individual measurements. However, it was difficult to accurately measure them due to the fine size of the particles, i.e., they are about 50–200 nm in size; hence, the pinning pressure of the Mo-rich precipitates cannot be determined in this study. It is shown in Table 8 that the pinning pressure from the MC carbides at 1080 and 1100 °C are estimated to be comparable, considering that the error bars are overlapping. Therefore, another large grain growth at 1100 °C that co-occurs with the dissolution of the Mo-rich precipitates strongly suggests that the pinning effect of dispersed fine Mo-rich precipitates plays a major role in inhibiting grain growth between 1020 and 1080 °C.

As shown earlier, the complete elimination of the Laves eutectics in K-TIG welded G27 with almost no formation of  $\eta$  platelets was achieved after a PWSHT at 1060 °C for 1 h, which is close to the dissolution temperature of the Laves phase in the FZ of TIG-welded ATI 718Plus as reported in Asala et al. [15], i.e. 1050 °C. It is plausible to assume that the complete removal of the Laves eutectic constituents in the FZ after welding may also be achieved in the same PWSHT conditions for the widely-used INCONEL® alloy 718, as the Nb content in INCONEL® alloy 718 is similar to that of ATI 718Plus. However, the PWSHT at 1060 °C is above the  $\delta$  phase solvus temperature, which is known to induce severe grain growth in the BM of INCONEL® alloy 718 that may deteriorate the mechanical properties. Fig. 18 shows that the grain growth kinetics of INCONEL® alloy 718 at 1060 °C is faster than that of G27, where a 1 h SHT led to a considerable increase in grain size from 29 to 88  $\mu\text{m}$ . G27 has a comparable initial grain size, so the grain size increased only from 25 to 59  $\mu\text{m}$  under the same SHT conditions, thus indicating a more significant inhibition of grain growth. The normal grain growth in the absence of the  $\delta$  phase in INCONEL® alloy 718 is controlled solely by the pinning effect of the (Nb, Ti)(C, N) particles [34]. In contrast, the finely dispersed Mo-rich precipitates in G27 are believed to contribute significantly to the pinning of grain boundaries during grain growth in addition to the pinning effect of the MC particles. Therefore, relative to INCONEL® alloy 718, the complete dissolution of the Laves eutectic constituents by using a PWSHT after welding to optimize the weld properties can be achieved without inducing excessive grain growth in

**Table 6**  
SEM-EDS analysis of plate-like phase in FZ and BM of post-weld solution heat-treated sample.

Element	Ni	Al	Ti	Nb	Mo	Cr	Fe
FZ (wt %)	72.26 ± 1.73	2.32 ± 0.20	4.54 ± 0.37	7.02 ± 0.58	1.81 ± 0.33	5.94 ± 1.25	6.11 ± 1.05
BM (wt %)	74.83 ± 1.23	2.38 ± 0.18	5.37 ± 0.54	6.44 ± 0.51	1.35 ± 0.36	4.56 ± 0.94	5.06 ± 0.78

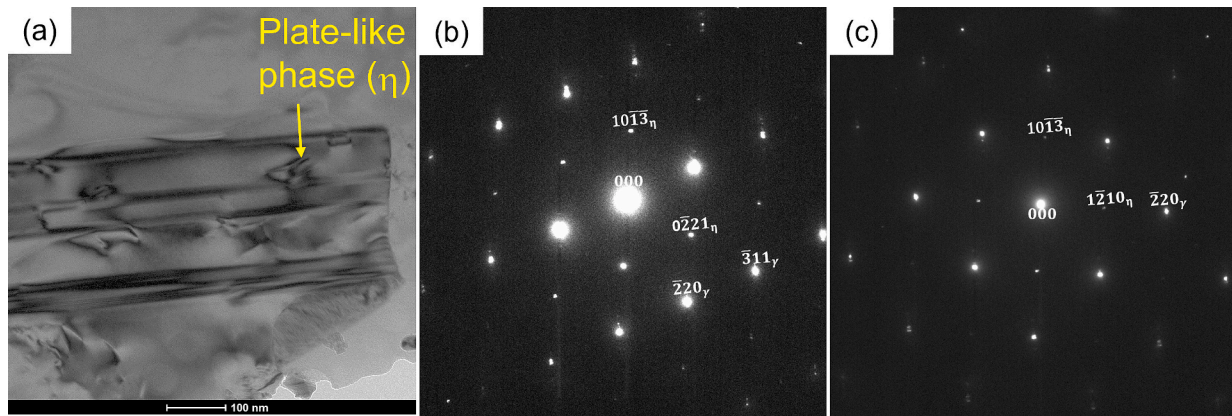


Fig. 14. (a) TEM BF image of  $\eta$  phase particles with corresponding SADPs which have zone axes parallel to (b)  $[112]_{\gamma}$  ( $[11476]_{\eta}$ ) and (c)  $[001]_{\gamma}$  ( $[3032]_{\eta}$ ).

Table 7

STEM-EDS analysis of plate-like phase ( $\eta$  phase) in post-weld solution heat-treated sample.

Element	Ni	Al	Ti	Nb	Mo	Cr	Fe
at%	73.59	6.07	8.73	7.32	0.67	1.39	2.24

the BM.

### 3.3.2. Identification of Mo-rich precipitates in BM of solution heat-treated G27

Due to the limitations of SEM-EDS in analysing sub-micron particles, extensive (S)TEM analyses were performed to identify the Mo-rich precipitates. Fig. 19(b) shows the STEM-EDS spectrum of a Mo-rich precipitate shown in a TEM BF image shown in Fig. 19(a), which reveals that the precipitate also contains Nb, Ni, Cr, Fe, and Si. The chemical composition of the Mo-rich precipitate obtained by a STEM-EDS analysis is listed in Table 9. It is shown that the ratio between (Ni + Cr + Fe) and (Mo + Nb + Si + Ti) in at.% is close to 2:1, thus suggesting that it exhibits a composition close to  $(\text{Ni, Cr, Fe})_2(\text{Nb, Mo, Ti})$  or  $\text{A}_2\text{B}$ . Thus, this is an indication that the Mo-rich precipitates could be the Laves phase.

TEM SADP analyses were then carried out to unambiguously identify the crystallographic nature of the Mo-rich precipitates. In this study, analyses of the SADPs obtained by systematic tilting of the Mo-rich precipitates to five different zone axes, as presented in Fig. 20, reveal that the precipitates are hexagonal close-packed Laves phase. It is also shown that all the tilt angles also match for a hexagonal close-packed crystal structure of the Laves phase. All experimental SADPs match the simulated diffraction patterns for the C14-Laves phase, as shown in the supplementary information (Fig. SI 1). The measured lattice parameters of the Mo-rich Laves phase are approximately  $a = 4.78 \text{ \AA}$ ,  $c = 7.76 \text{ \AA}$ , which are very close to those of the Nb-rich irregular-shaped Laves phase formed as a solidification product in the FZ of the as-welded G27 in this work and as-welded ATI 718Plus reported in Asala et al. [15]. In addition, It is worth noting that planar stacking faults were observed, as shown by the bright streaks within the Mo-rich laves phase particle shown in Fig. 20(a), which is a typical characteristic feature of Laves phase and consistent with the literature on laves phases [35,36]. A high-magnification TEM image that shows the presence of planar stacking faults within the Mo-rich Laves phase is shown in the supplementary information (Fig. SI 2).

Additional confirmation of the crystallographic structure of the Mo-rich Laves phase was made through a convergent beam electron

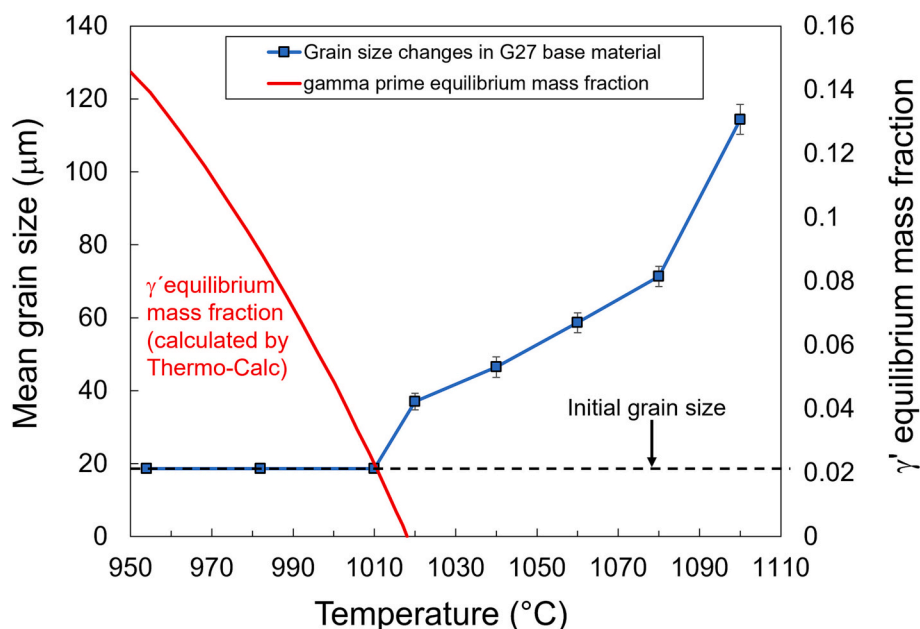


Fig. 15. Changes in grain size of BM with SHT temperature and  $\gamma'$  equilibrium mass fraction calculated with Thermo-Calc.



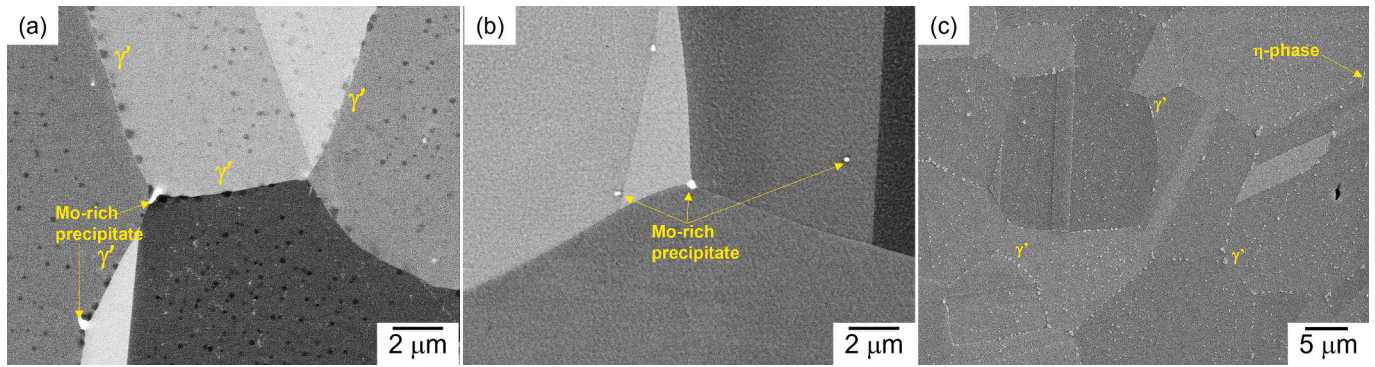


Fig. 16. SEM-BSE micrographs of samples that are solution heat treated at (a) 1010 °C and (b) 1020 °C observed on as-polished surfaces; (c) secondary electron (SE) micrograph of etched sample solution heat treated at 1010 °C that shows low density of  $\eta$  phase on grain boundaries.

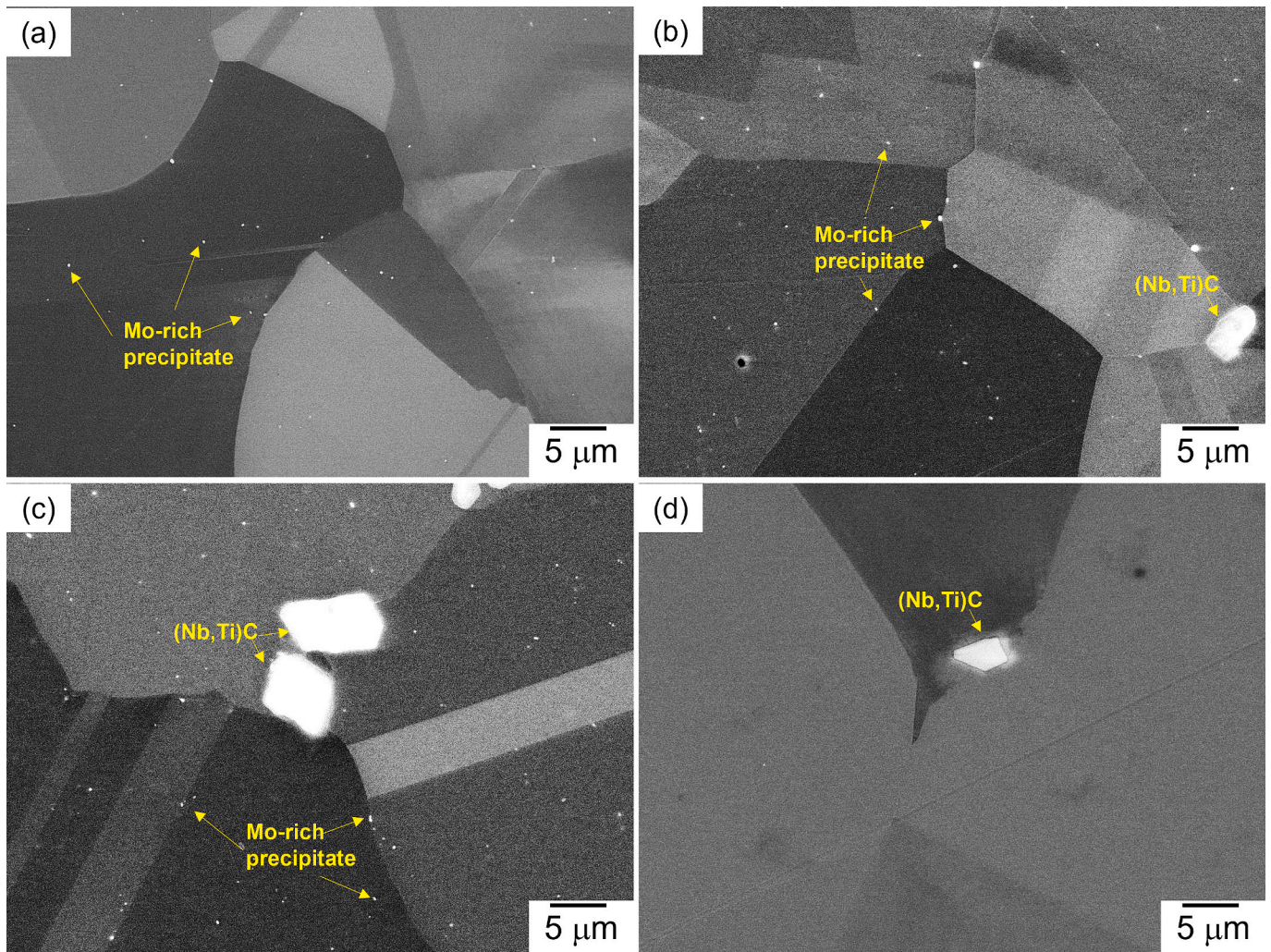


Fig. 17. SEM BSE micrographs of BM of sample solution heat-treated at (a) 1020 °C, (b) 1060 °C, (c) 1080 °C, and (d) 1100 °C.

Table 8

Average  $A_f$ ,  $r$ , and calculated  $P_z$  for MC carbides obtained from SHT at 1080 °C and 1100 °C. The error bars of  $P_z$  are obtained from the error bars of  $A_f$ .

SHT condition	$A_f$ (%)	$r$ ( $\mu\text{m}$ )	$P_z$ (MPa)
1080 °C/1 h	$0.43 \pm 0.09$	2.8	$0.0019 \pm 0.0004$
1100 °C/1 h	$0.40 \pm 0.06$	2.6	$0.0019 \pm 0.0003$

diffraction (CBED) analysis (Fig. 21(a-c)). The CBED technique involves the use of a highly convergent beam of electrons to obtain the diffraction information from a tiny area (1 to 2 nm) in contrast to selected area diffraction, where a parallel beam is used to obtain the diffraction information from a comparatively and considerably larger area. CBED is used to determine the crystallographic point group of a crystal and space groups based on the symmetries of the CBED patterns acquired in close-packed directions. According to the International Tables for



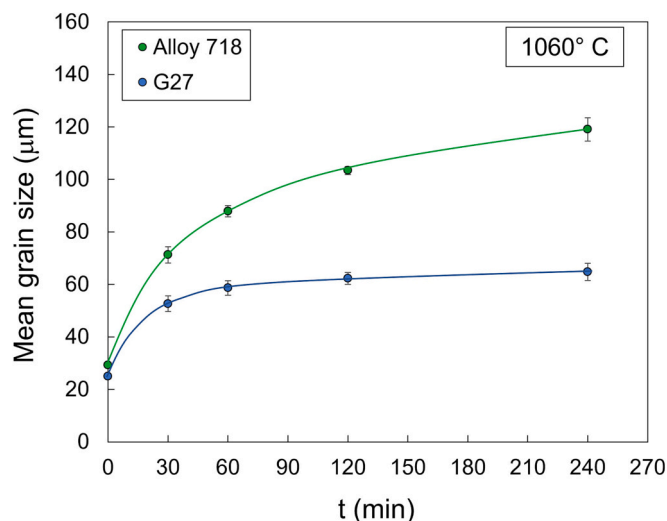


**Fig. 18.** Change in grain size versus soaking time during SHT at 1060 °C in the BM of G27 and Inconel alloy 718.

Crystallography, 6/mmm is the only point group consistent in all the symmetries of the zone axes. The 6/mmm point group is the common point group that also provides the P63/mmc space group of the Laves phase.

The positive identification of the Mo-rich Laves phase particles in the BM of solution heat-treated G27, which is made possible by the detailed (S)TEM analyses carried out in this work, has led to speculation whether they might be remnants of the Laves phase particles that remain undissolved on the as-received plate from the as-cast alloy that had undergone homogenization and hot rolling process. However, based on our careful SEM-EDS analysis, no evidence of Mo-rich Laves phase particles can be found in the as-received G27 plate, which suggests that they likely formed during the SHT. In order to confirm this assertion, additional SHTs were performed on the BM of G27. The sample was first solution heat-treated at 1133 °C for 5 min to dissolve all of the second-phase particles except for the MC carbides, followed by water quenching. Then, the sample was subsequently solution heat-treated at 1040 °C for 1 h followed by water quenching. Fig. 22(a) shows the SEM BSE image of the sample quenched after reaching a temperature of 1133 °C, where the SHT results in significant grain growth. The grain size is larger

than 100 μm and the microstructure is free of the Mo-rich Laves phase. Fig. 22(b) shows that after the second SHT step at 1040 °C for 1 h, the presence of the Mo-rich Laves phase is observed. This observation suggests that they are precipitated from a solid state during the SHT. However, in contrast to the randomly dispersed phase particles in the solution heat-treated microstructure shown in Fig. 17, the Mo-rich Laves phase particles shown in Fig. 22(b) are precipitated on the grain boundaries. The difference in the spatial distribution of the Mo-rich Laves phase during their formation is still unclear and needs further investigation.

It is well-known that Laves phase is formed from the liquid in Nb-bearing Ni-based superalloys during solidification in casting, welding and additive manufacturing (AM). This type of Laves phase is typically Nb-rich and irregularly shaped. However, in contrast to the irregular-shaped Nb-rich Laves phase formed from liquid, the Laves phase particles identified in the BM of G27 in this work are Mo-rich, have a granular morphology, and formed during the short-term SHT through solid-state precipitation. To the best of our knowledge, the solid-state precipitation of the Mo-rich Laves phase observed in this study during heat treatment has not been reported in any commercial Ni-based superalloys subjected to a short-term heat treatment, as used in the present work; it has been reported primarily in INCONEL® alloy 718 [37,38] and ATI 718 Plus [35], during long-term heat treatment. Apart from the exposure time needed during heat treatment to form the Mo-rich Laves phase, another notable difference is that the Mo-rich Laves phase reported in INCONEL® alloy 718 [37,38] and ATI 718 Plus [35] are formed at a temperature range much lower (650–788 °C) than heat treatment temperatures used in this study for G27 (950–1080 °C). An equilibrium phase diagram calculation was performed by using Thermo-Calc (Fig. 23) to confirm the stability of the Mo-rich Laves phase in G27. However, the stability of the Laves phase cannot be ensured at temperatures between 940 and 1100 °C because either the TTNI8 thermodynamic database is inaccurate or the system has not reached equilibrium, i.e. the Mo-rich Laves phase might be metastable. Again, this needs to be further studied in future work to elucidate the nature of the Mo-rich Laves phase and its formation in G27.

#### 4. Summary and conclusions

1. Secondary interdendritic microconstituents in the FZ of as-welded G27 are identified as Nb-rich MC carbides, Nb-rich irregular Laves

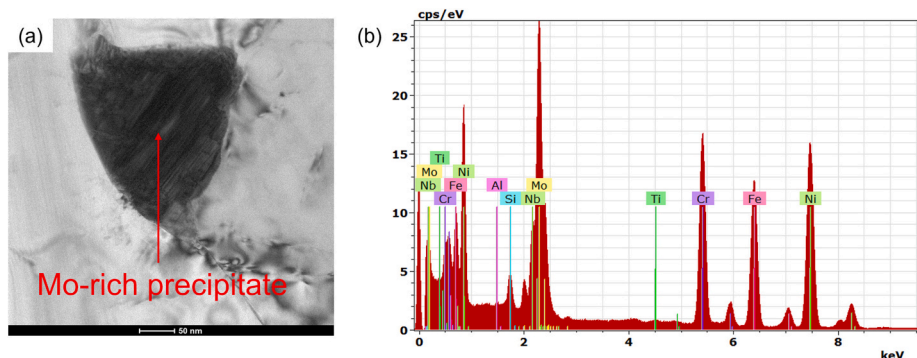


**Fig. 19.** (a) TEM-BF image of Mo-rich precipitate, and (b) STEM-EDS spectrum of the precipitate in (a).

**Table 9**

Chemical composition of the Mo-rich precipitates obtained by STEM-EDS analysis on the precipitate in Fig. 17(a).

Element	Ni	Al	Ti	Nb	Mo	Cr	Fe	Si
wt%	21.85	0.34	0.38	11.95	33.00	16.19	14.47	1.82
at%	24.81	0.84	0.52	8.57	22.92	20.74	17.27	4.82



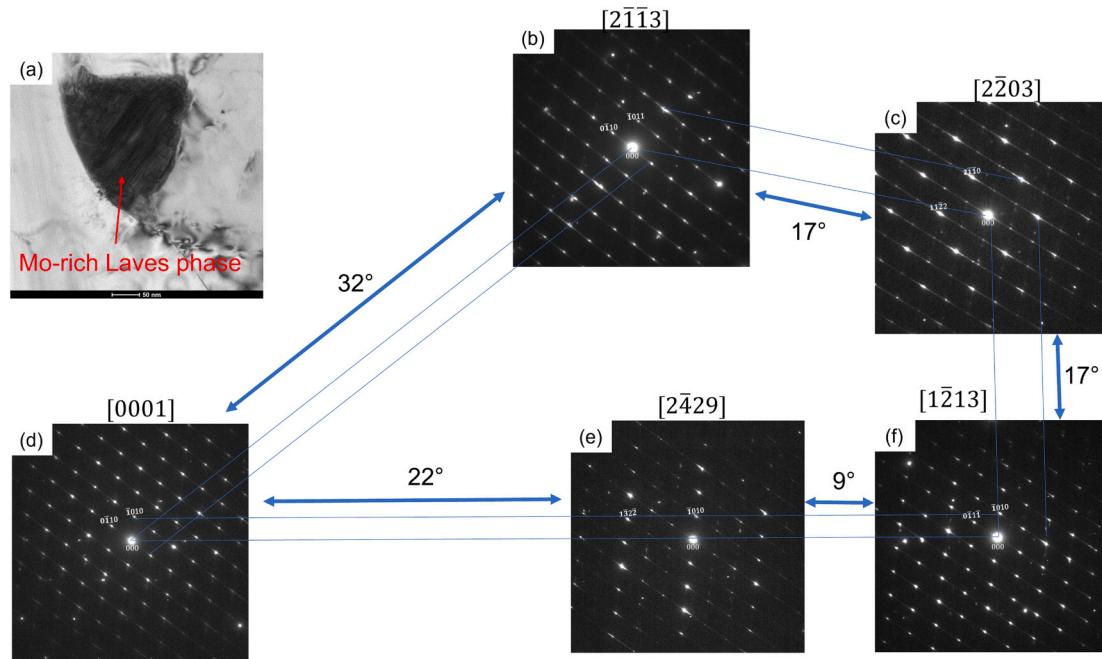


**Fig. 20.** (a) TEM BF image of Mo-rich Laves phase with corresponding SADPs of five different zone axes shown in (b)–(f) where all the tilt angles also match for a hexagonal close-packed crystal structure of Laves phase.

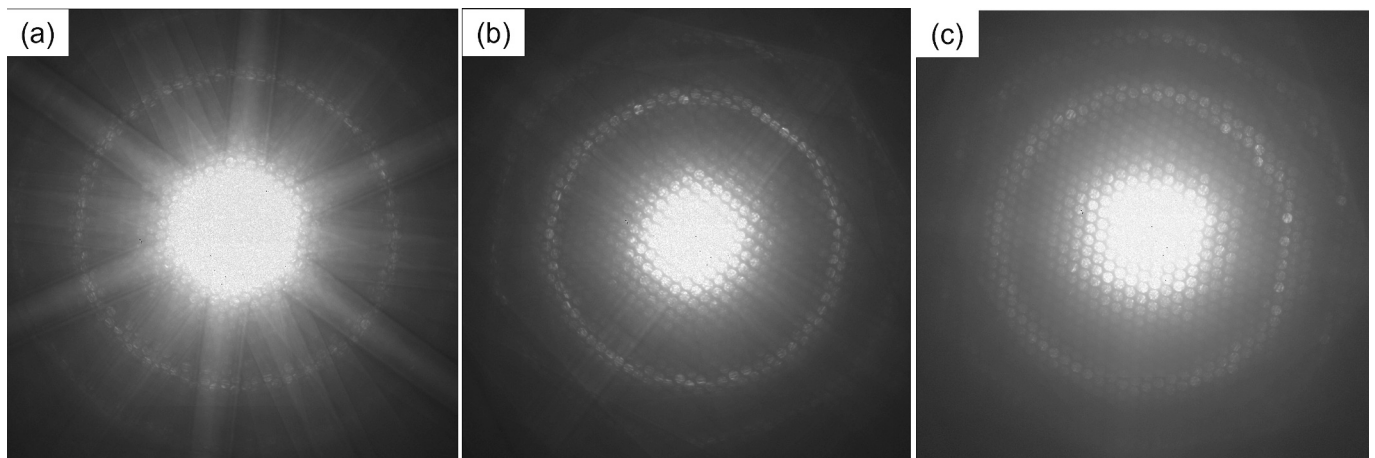


**Fig. 21.** Convergent electron diffraction patterns of the (a) [0001], (b) [2113], and (c) [1213] zone axes, which show 6 mm, 2 mm, and 2 mm whole pattern symmetry, respectively.

- eutectics, and  $\gamma'$ , and  $\eta$  phase particles, where the solidification phases include MC, Laves eutectics and possibly the  $\eta$  phase.
- PWSHTs are performed to avoid the potentially deleterious effects of the irregular Laves eutectics on the mechanical properties of the weld. A PWSHT carried out between 954 and 1010 °C results in only partial removal of the Laves phase particles with excessive formation of the  $\eta$  phase around the Laves particles, which could potentially have more negative effects on the mechanical properties. Complete dissolution of irregular-shaped Laves eutectics with no  $\eta$  phase formation is achieved after implementation of a PWSHT at 1060 °C.
  - The grain growth behavior in the BM of G27 during SHT has been characterized. The fine grain size of 20  $\mu\text{m}$  remains unchanged after SHTs up to 1010 °C due to the grain boundary pinning by the  $\gamma'$  precipitates. In the absence of  $\gamma'$ , SHTs between 1020 and 1080 °C results in grain growth from 37 to 71  $\mu\text{m}$ , which is believed that the pinning effect of the Mo-rich precipitates controls the grain growth.

- Relative to INCONEL® alloy 718, the complete dissolution of the Laves eutectic constituents in the weld FZ of G27 after a PWSHT at 1060 °C can be achieved without causing excessive grain growth in the BM, which is likely attributed to the pinning effect of the Mo-rich precipitates.
- The Mo-rich precipitates are identified as a Mo-rich hexagonal close-packed Laves phase after extensive (S)TEM analyses are carried out.
- The Mo-rich Laves phase in the BM of G27 is formed through a solid state precipitation during SHT, which has not been reported in any commercial Ni-based superalloys subjected to short-term SHT, as used at the present work.

#### Declaration of Competing Interest

The authors declare no potential conflict of interest.

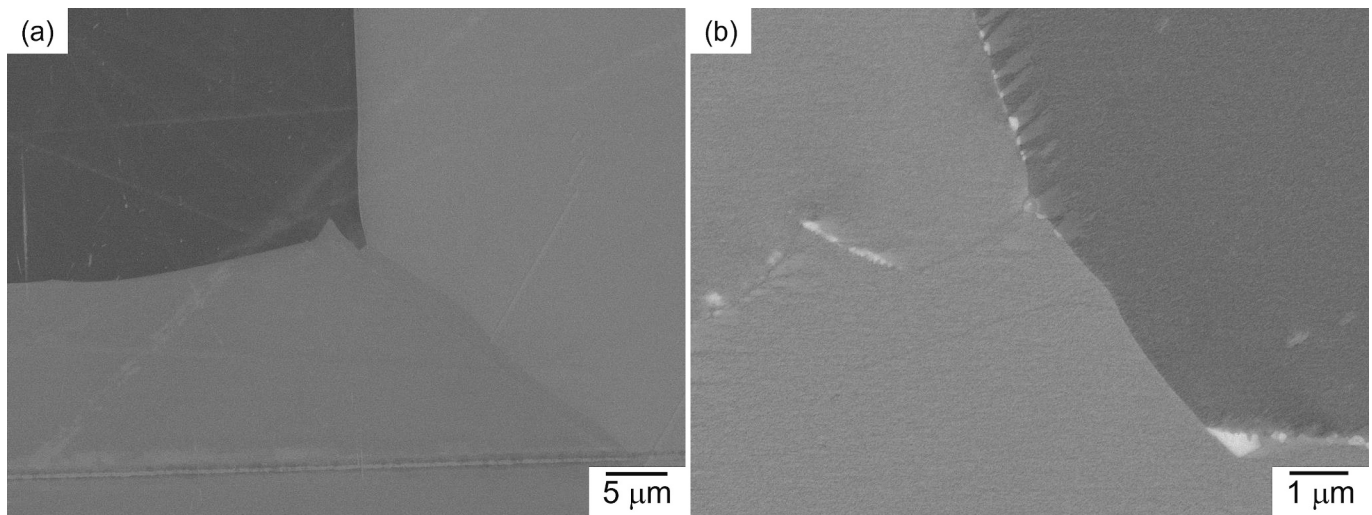


Fig. 22. SEM BSE micrographs of (a) as-solution heat-treated at 1133 °C/5 min and (b) as solution heat-treated at 1133 °C/5 min + 1040 °C/1 h.

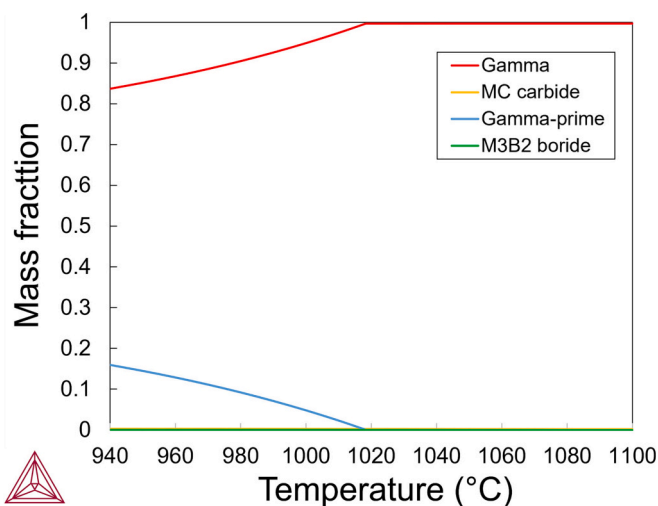


Fig. 23. Equilibrium phase diagram calculated by using Thermo-Calc with nominal alloy composition of G27.

#### Data availability

No data was used for the research described in the article.

#### Acknowledgment

This work is based on the research within the FEAST (Weld Feasibility Heat Treatment Studies of New Superalloys, registration number: 2019-02787) project funded by the Swedish funding agency VINNOVA. We greatly appreciate the support and input from Dr. Ceena Joseph, Mr. Bengt Pettersson, and Mr. Fredrik Olofsson at Brogren Industries AB. We also appreciate the support from Carpenter Technology Corporation in providing the materials. Special acknowledgment to Mattias Igstrand of University West for performing the K-TIG welding operations. Immense help from Dr. Yiming Yao at the Chalmers University of Technology for the electropolishing of the STEM samples is greatly appreciated.

#### Appendix A. Supplementary data

Supplementary data to this article can be found online at <https://doi.org/10.1016/j.matchar.2023.113178>.

#### References

- [1] K.A. Heck, N. Zhou, S.J. Kernion, D. Rickert, F. Van Weereld, A new co-free Ni-based alloy for gas turbine and exhaust valve applications, in: *Superalloys 2020*, Springer, 2020, pp. 142–152, [https://doi.org/10.1007/978-3-030-51834-9\\_14](https://doi.org/10.1007/978-3-030-51834-9_14).
- [2] J. Andersson, Review of weldability of precipitation hardening Ni- and Fe-Ni-based superalloys, in: *Proceedings of the 9th International Symposium on Superalloy 718 & Derivatives: Energy, Aerospace, and Industrial Applications*, Springer, 2018, pp. 899–916, [https://doi.org/10.1007/978-3-319-89480-5\\_60](https://doi.org/10.1007/978-3-319-89480-5_60).
- [3] S. Cui, Z. Liu, Y. Fang, Z. Luo, S.M. Manladan, S. Yi, J. Mater. Process. Technol. 243 (2017) 217–228, 0924-0136, <https://doi.org/10.1016/j.jmatprotec.2016.12.027>, 0924-0136.
- [4] Z. Fei, Z. Pan, D. Cuiuri, H. Li, S. Van Duin, Z. Yu, J. Manuf. Process. 45 (2019) 340–355, 1526-6125, <https://doi.org/10.1016/j.jmapro.2019.07.017>, 1526-6125.
- [5] Z. Fei, Z. Pan, D. Cuiuri, H. Li, B. Wu, D. Ding, L. Su, A.A. Gazder, J. Manuf. Process. 32 (2018) 482–493, 1526-6125, <https://doi.org/10.1016/j.jmapro.2018.03.014>, 1526-6125.
- [6] C.H. Radhakrishna, K. Prasad Rao, J. Mater. Sci. 32 (1997) 1977–1984, 1573-4803, <https://doi.org/10.1023/A:1018541915113>, 1573-4803.
- [7] T. Sonar, V. Balasubramanian, S. Malarvizhi, T. Venkateswaran, D. Sivakumar, Mater. Charact. 174 (2021) 110997, 111044-115803, <https://doi.org/10.1016/j.matchar.2021.110997>, 111044-115803.
- [8] T. Sonar, V. Balasubramanian, T. Venkateswaran, V. Xavier, M. Agilan, A. Manjunath, M. Ivanov, I. Suleymanova, Mater. Sci. Eng. A (2023) 145323, 140921-145093, <https://doi.org/10.1016/j.msea.2023.145323>, 140921-145093.
- [9] G.D.J. Ram, A.V. Reddy, K.P. Rao, G.M. Reddy, J.K.S. Sundar, J. Mater. Process. Technol. 167 (2005) 73–82, 0924-0136, <https://doi.org/10.1016/j.jmatprotec.2004.09.081>, 0924-0136.
- [10] P.N. Quested, M. McLean, *Solidification Technology in the Foundry and Cast House*, 1980, pp. 586–591.
- [11] L. Ling, Y. Han, W. Zhou, H. Gao, D. Shu, J. Wang, M. Kang, B. Sun, Metall. Mater. Trans. A 46 (2015) 354–361, 1073-5623, <https://doi.org/10.1007/s11661-014-2614-5>, 1073-5623.
- [12] J. DuPont, A. Marder, M. Notis, C. Robino, Metall. Mater. Trans. A 29 (1998) 2797–2806, <https://doi.org/10.1007/s11661-998-0320-x>.
- [13] T.F. Bower, Trans. Metall. Soc. AIME 236 (1966) 624–634.
- [14] D.F. Paulonis, J.M. Oblak, D.S. Duvall, *Precipitation in Nickel-Base Alloy 718*, Pratt and Whitney Aircraft, Conn, Middletown, 1969.
- [15] G. Asala, J. Andersson, O.A. Ojo, Int. J. Adv. Manuf. Technol. 87 (2016) 2721–2729, <https://doi.org/10.1007/s00170-016-8642-0>.
- [16] O. Ojo, N. Richards, M. Chaturvedi, Metall. Mater. Trans. A 37 (2006) 421–433, <https://doi.org/10.1007/s11661-006-0013-2>.
- [17] G. Knorovsky, M. Cieslak, T. Headley, A. Romig, W. Hammetter, Metall. Trans. A. 20 (1989) 2149–2158, <https://doi.org/10.1007/BF02650300>.
- [18] R.G. Thompson, D.E. Mayo, B. Radhakrishnan, Metall. Trans. A. 22 (1991) 557–567, 0360-2133, <https://doi.org/10.1007/BF02656823>, 0360-2133.
- [19] A. Ariasetta, D. Pick, J. Andersson, O. Ojo, Keyhole TIG Welding of New Co-Lean Nickel-Based Superalloy G27, Springer Nature Switzerland, Cham, 2023, pp. 807–824, [https://doi.org/10.1007/978-3-031-27447-3\\_48](https://doi.org/10.1007/978-3-031-27447-3_48), 978-3-031-27447-3.
- [20] E. Pickering, H. Mathur, A. Bhowmik, O. Messé, J. Barnard, M. Hardy, R. Krakow, K. Loehnert, H. Stone, C. Rae, Acta Mater. 60 (2012) 2757–2769, <https://doi.org/10.1016/j.actamat.2012.01.042>.
- [21] F. Laves, H.J. Wallbaum, *Zeitschrift für Kristallographie-Crystalline Materials* 101 (1939) 78–93, 2196-7105.
- [22] K. Vishwakarma, N. Richards, M. Chaturvedi, Mater. Sci. Eng. A 480 (2008) 517–528, <https://doi.org/10.1016/j.msea.2007.08.002>.

- [23] H.L. Eiselstein, D.J. Tillack, Superalloys 718 (1991) 1–14, [https://doi.org/10.7449/1991/superalloys.1991\\_1\\_14](https://doi.org/10.7449/1991/superalloys.1991_1_14).
- [24] J.N. DuPont, M. Notis, A. Marder, C. Robino, J. Michael, Metall. Mater. Trans. A 29 (1998) 2785–2796, <https://doi.org/10.1007/s11661-998-0319-3>.
- [25] M. Cieslak, G. Knorovsky, T. Headley, A. Romig Jr., The Solidification Metallurgy of Alloy 718 and Other Nb-Containing Superalloys, Sandia National Lab.(SNL-NM), Albuquerque, NM (United States), 1989, [https://doi.org/10.7449/1989/Superalloys.1989\\_59\\_68](https://doi.org/10.7449/1989/Superalloys.1989_59_68).
- [26] J.J. Schirra, R.H. Caless, R.W. Hatala, Superalloys 718 (1991) 375–388, [https://doi.org/10.7449/1991/SUPERALLOYS.1991\\_375\\_388](https://doi.org/10.7449/1991/SUPERALLOYS.1991_375_388).
- [27] L.A. James, Weld. J. Res. Suppl. 57 (1978) 17s–23s.
- [28] L.C.M. Valle, L.S. Araújo, S.B. Gabriel, J. Dille, L.H. De Almeida, J. Mater. Eng. Perform. 22 (2013) 1512–1518, 1059-9495, <https://doi.org/10.1007/s11665-012-0433-7>, 1059-9495.
- [29] S. Antonov, M. Detrois, R.C. Helmink, S. Tin, J. Alloys Compd. 626 (2015) 76–86, 0925-8388, <https://doi.org/10.1016/j.jallcom.2014.11.155>, 0925-8388.
- [30] D. Collins, B. Conduit, H. Stone, M. Hardy, G. Conduit, R. Mitchell, Acta Mater. 61 (2013) 3378–3391, <https://doi.org/10.1016/j.actamat.2013.02.028>.
- [31] K. Song, M. Aindow, Mater. Sci. Eng. A 479 (2008) 365–372, <https://doi.org/10.1016/j.msea.2007.09.055>.
- [32] M. Pa, M. Ferry, T. Chandra, ISIJ Int. 38 (1998) 913–924, 0915-1559, <https://doi.org/10.2355/isijinternational.38.913>, 0915-1559.
- [33] M.-A. Charpagne, J.-M. Franchet, N. Bozzolo, Mater. Des. 144 (2018) 353–360, 0264-1275, <https://doi.org/10.1016/j.matdes.2018.02.048>, 0264-1275.
- [34] G. Muralidharan, R.G. Thompson, Scr. Mater. 36 (1997) 755–761, 1359-6462, [https://doi.org/10.1016/S1359-6462\(96\)00450-2](https://doi.org/10.1016/S1359-6462(96)00450-2), 1359-6462.
- [35] R. Krakow, D.N. Johnstone, A.S. Eggeman, D. Hünert, M.C. Hardy, C.M.F. Rae, P. A. Midgley, Acta Mater. 130 (2017) 271–280, 1359-6454, <https://doi.org/10.1016/j.actamat.2017.03.038>, 1359-6454.
- [36] S. Staroń, B. Dubiel, K. Gola, I. Kalembe-Rec, M. Gajewska, H. Pasiowicz, R. Wrobel, C. Leinenbach, Metall. Mater. Trans. A 53 (2022) 2459–2479, 1073-5623, <https://doi.org/10.1007/s11661-022-06679-1>, 1073-5623.
- [37] S.J. Sijbrandij, M.K. Miller, J.A. Horton, W.D. Cao, Mater. Sci. Eng. A 250 (1998) 115–119, 0921-5093, [https://doi.org/10.1016/S0921-5093\(98\)00546-2](https://doi.org/10.1016/S0921-5093(98)00546-2), 0921-5093.
- [38] D. Srinivasan, Mater. Sci. Eng. A 364 (2004) 27–34, 0921-5093, <https://doi.org/10.1016/j.msea.2003.06.003>, 0921-5093.